

Confrontations of Non-Standard Physics Models with Cosmic Microwave Background Data

CHAN, Kwan Chuen

A Thesis Submitted in Partial Fulfillment
of the Requirements for the Degree of
Master of Philosophy
in
Physics

©The Chinese University of Hong Kong
July 2007

The Chinese University of Hong Kong holds the copyright of this thesis. Any person(s) intending to use a part or the whole of the materials in this thesis in a proposed publication must seek copyright release from the Dean of the Graduate School.

Abstract

We are now in the era of precision cosmology. Large volume of precise cosmological data are obtained from many experiments and observations. In particular the Wilkinson Microwave Anisotropies Probe (WMAP) measures the Cosmic Microwave Background (CMB) Anisotropies to high precision. We are now able to put various extensions of standard model to scrutiny. This means that some models can be ruled out or the model parameters will be limited to certain ranges. In this thesis, we make use of current cosmological data, mainly the WMAP CMB data to constrain some models of generalization of general relativity and string theory motivated origin.

One possible generalization of general relativity is that the gravitational constant G can be varying. In Chapter 3, we use the CMB power spectra to constrain the cosmological variation of G from redshift $z \approx 1000$ to 0. The constraint is parametrization dependent, and the bound on \dot{G}/G is about $(-9.6 \sim 8.1) \times 10^{-12} \text{ yr}^{-1}$.

In Chapter 4, we consider another generalization to GR, the $f(R)$ gravity in the Palatini formalism. The particular form we study is $f(R) = R + \alpha|R|^\beta$. Using the CMB power spectrum, matter power spectrum and the supernovae data, we are able to constrain the model parameter β to the order $\sim \mathcal{O}(10^{-6})$, so that the modified gravity theory is nearly indistinguishable from the standard Λ CDM model.

Finally, in Chapter 5, we use the WMAP data to constrain the evolution of the extra dimension volume, the radion, in brane model. In many versions

of brane model, the radion could have cosmological evolution, which induces variation of the Higgs vacuum expectation value, $\langle H \rangle$, resulting in cosmological variation of the electron mass m_e . We obtain a constraint on ρ , the ratio of the value of $\langle H \rangle$ at CMB recombination to its present value, to be $[0.97, 1.02]$.

Acknowledgments

First of all I would like to express my great gratitude to my thesis advisor Prof. Chu Ming-Chung for his illuminating instructions. Many of his insightful ideas ultimately crystallize to important ingredients of this work. He always prods me to higher level of clarity in presentation (of course I am fully responsible for any ambiguities in this thesis!). In addition to Prof. Chu, I also learned a lot from other teachers at our department during my undergraduate and M Phil studies, in particular my M Phil teachers Prof. H. M. Lai, K. L. Liu and P. M. Hui. Here I want to thank them for their patient teaching.

I am also grateful to our former and present group members for useful discussions and assistance. Among them I especially benefited from communications with our former group member B. Li.

Most of the computations are done using the computers at the ITSC of the Chinese University of Hong Kong. Without those hard-working helpers and the officer Frank Ng at ITSC, I would have been forced to work as a computer technician. I would like to express my thanks to those helped me compile and run the codes.

I appreciate the willingness of Prof. P. M. Hui, C. K. Law and the external examiner to work as my examiners even though they are very busy.

Last but not least, in the last couple of years, I was so concentrated in my own academic activities that I neglected many intimate people around me. I am very sorry for them, and I have paid. I lost my girlfriend partly because I did not pay enough attention to her. My father passed away two months

ago, but, regretably, I did not take good care of him when he was ill. If I had anticipated those consequences I would have stolen less private time. To express my remorse and respect for my father, I dedicate this thesis to the memory of my beloved father, who had devoted his life to the family.

Contents

1	Overview of Cosmology	1
1.1	Friedmann-Robertson-Walker Universe	1
1.2	The Hubble Diagram and Type Ia Supernovae	3
1.3	Big Bang Nucleosynthesis	5
1.4	Cosmic Microwave Background	8
1.5	Matter Power Spectrum and Galaxy Surveys	10
1.6	The Energy Density Budget of the Universe and Outlook	13
2	Review of CMB Physics	17
2.1	Main Physics of the CMB Power Spectra	17
2.1.1	Photon-Baryon Fluid	17
2.1.2	Initial Conditions	20
2.1.3	Acoustic Peaks	22
2.1.4	Baryons in Action	23
2.1.5	Damping	24
2.1.6	Polarization	25
2.2	Computation of CMB Power Spectrum	26
3	Constraints on Variation of the Gravitational Constant by CMB	30
3.1	Current Constraints on G and Theoretical Motivations	31
3.2	Parametrization of G	32

3.3	Effect of Variation of G on the CMB Temperature and Polarization Power Spectra	34
3.4	Constraining G by MCMC and Discussions	40
3.5	Conclusion	45
4	Constraints on $f(R)$ Cosmology in the Palatini Formalism	47
4.1	Introduction	48
4.2	Field Equations in Theories of Palatini - $f(R)$ Gravity	50
4.2.1	General Theory of $f(R)$ Gravity in the Palatini Approach	50
4.2.2	The Perturbation Equations	52
4.3	Numerical Results and Cosmological Constraints	56
4.4	Discussion and Conclusion	62
5	CMB Constraint on Radion Evolution in the Brane World Scenario	65
5.1	Introduction	66
5.2	Dimensional Reduction and Low Energy Effective Actions	68
5.3	Numerical Constraints on the Evolution of the Radion	72
5.3.1	Effects of Variation of Higgs VEV on CMB Power Spectra	72
5.3.2	Numerical Constraints on the Higgs VEV and Radion by CMB	75
5.4	Conclusion	80
6	Summary of the Thesis	81
A	Markov Chain Monte Carlo Method	84
A.1	Basic Theory of MCMC	84
A.2	The Metropolis-Hastings Algorithm	86
A.3	Convergence Diagnostics	87
B	Forecast by Fisher Matrix	89

C Modified Equations in RECFAST with Variation m_e	92
Bibliography	95

List of Figures

1.1	Hubble diagram obtained by the HST Key Project [1]. Five different distance measures are used to estimate distance. Relative to other measures SNe Ia extends the observable distance by a factor of 2. They collectively indicate that $H_0 = 72 \pm 8 \text{ km s}^{-1} \text{ Mpc}^{-1}$	4
1.2	Hubble diagram from SCP [2]. In the upper panel, the effective magnitude is plotted against the redshift. The solid curve ($\Omega_\Lambda = 0.75$) fits the data much better than those with $\Omega_\Lambda = 0$. The lower panel shows the residuals relative to an empty universe ($\Omega_\Lambda = 0, \Omega_M = 0$), illustrating how strong the dark energy has been detected.	6
1.3	The BBN prediction of abundance of ^4He , deuterium, ^3He and ^7Li as a function of baryon density. The bands are due to uncertainties in theoretical calculations. The boxes and arrows represent the 95% abundance limits from observations, and the vertical strip indicates the constraints from the measurement of primordial deuterium alone. This figure is taken from Ref. [3].	7
1.4	The three-year WMAP temperature anisotropy map. Spots are fluctuations in the CMB temperature across the celestial sphere. The magnitude of fluctuations $\delta T/T$ is of the order of 10^{-5} . The figure is taken from [4].	9

1.5	The temperature power spectrum from three-year WMAP, together with other ground/balloon experiments dedicated to measuring high- l spectrum. The solid line represents the best fit Λ CDM model. This figure is taken from [4].	10
1.6	The distribution of main galaxies (grey/green) and Luminous Red Galaxies (LRG) in SDSS [5]. These two types of galaxies are singled out from the SDSS dataset for further analysis. The measured LRGs are as far as $z \sim 0.5$. This image of large scale structures provides a glimpse of the primordial fluctuations spectrum and enables us to constrain the cosmological parameters, especially Ω_M	12
1.7	Measured power spectra from the LRG and main galaxy samples. The solid lines are the best fit linear Λ CDM models, while the dashed lines include nonlinear corrections. The galaxy bias b are different for these two types of galaxies. This figure is taken from the SDSS collaboration [5].	13
3.1	The CMB temperature angular power spectra for three values of the Newtonian gravitational constant with instantaneous stabilization $z_s = 0$. The solid, dotted and dashed curves correspond to $\lambda_0^2 = 1, 0.5$ and 3 respectively. The damping effect is only noticeable for $l > 500$	35
3.2	Same as Fig. 3.1 but with spectra with $z_s = 10$ in contrast with those with $z_s = 0$. The standard spectrum (solid) nearly coincides with the one with $\lambda_0^2 = 1.2$ and $z_s = 0$ (dot-dashed). When instantaneous stabilization occurs at $z_s = 10$, marked shifts to larger (smaller) l scales result for $\lambda_0^2 = 1.2$ (dotted) (0.8 (dashed)).	36

3.3	The E-polarization spectra with instantaneous stabilization at $z_s = 0$ and 10. The peaks shift to larger (smaller) l scales for $\lambda_0^2 = 2$ (0.6) when instantaneous stabilization takes place at $z_s = 10$, in contrast to the cases without stabilization ($z_s = 0$).	37
3.4	The effects of linear variation of G on the temperature power spectrum. The solid line shows the spectrum when there is no variation of G . When $\lambda_0^2 = 1.2$ (0.8), the peaks shift to larger (smaller) l scales. a_s is set to be 1.	38
3.5	The left (right) panel shows $\delta l_n/n = \pi\delta(d_*/r_s)$ vs. λ_0^2 for instantaneous (linear) stabilization. For the plot on the left, the thick (red) solid curve corresponds to $a_s=0.1$ and the dashed curve to $a_s=0.5$. The dots correspond to $\delta l_n/n$ averaged over the first three peaks of the spectra in Fig. 3.2 ($\lambda_0^2 = 1.2, z_s = 10$ and $\lambda_0^2 = 0.8, z_s = 10$). The two thin solid (black) curves are obtained using the simplified formula Eq. 3.16 for $a_s = 1$ and 0.5 respectively. On the right, the solid and dashed curves correspond to linear stabilization with $a_s = 1$ and 0.5 respectively. Similarly we denote by the dots the average $\delta l_n/n$ in Fig. 3.4 for $a_s = 1$, and $\lambda_0^2=1.2$ and 0.8 respectively.	40
3.6	The marginal distributions of λ_0^2 and $\ln z_s$ obtained using the three-year WMAP data set in the instantaneous stabilization scenario. Here and thereafter, the maximum of the distribution is normalized arbitrarily to 1.	41
3.7	The contour plot of the joint distribution of λ_0^2 and $\ln z_s$ constrained using the three-year WMAP data set in the instantaneous stabilization scenario. The inner and outer solid lines are the 68% and 95% confidence level contours respectively.	42
3.8	The marginal distributions of λ_0^2 for the linear stabilization scenario in Eq. 3.3 with $z_s = 0$ and $z_s = 0.8$ respectively, constraint using the three-year WMAP data.	43

4.1	The TT CMB spectrum for the $f(R) = R + \alpha(-R)^\beta$ model, with Ω_m (current fractional energy density of nonrelativistic matter) and H_0 (current Hubble constant) fixed to be 0.3 and 72 km/s/Mpc respectively. Choices of β are indicated besides the curves. The case $\beta = 0$ corresponds to a Λ CDM Universe.	56
4.2	The matter power spectra of the $f(R) = R + \alpha(-R)^\beta$ model for different choices of β (both negative and positive) as indicated beside the curves. The case $\beta = 0$ corresponds to a Λ CDM Universe.	58
4.3	The marginal distributions of Ω_m and β , obtained using the three year WMAP data alone. Here the distributions are normalized such that the maximum probability density is 1.	59
4.4	The contour plot of the joint distribution of Ω_m and β , constrained by WMAP data alone. The inner and outer loops are the 68% and 95% confidence contours respectively.	59
4.5	The marginal distributions of the various model parameters, constrained simultaneously by the WMAP, SNLS and SDSS data sets. The distributions are normalized such that the maximum probability density is 1.	60
4.6	The contour plot of joint distribution of Ω_m and β under the constraints of the WMAP, SNLS and SDSS data sets. The inner and outer loops are the 68% and 95% confidence contours respectively.	61
4.7	The data points from SNLS (upper panel), WMAP (middle panel) and SDSS (lower panel) data sets against the theoretical curves of our best-fitted model. For SDSS data we have plotted both vertical and horizontal error bars. Note that the last three data points from SDSS (for which $k > 0.2h \text{ Mpc}^{-1}$) are not included in our numerical constraints, and we have used a bias of 1.1 to relate the best fit theoretical power spectrum to the SDSS data.	64

5.1	The CMB temperature power spectrum with $\rho=1, 1.05$ and 0.95 respectively. Other cosmological parameters assume the standard values.	74
5.2	The CMB E -polarization power spectrum with $\rho=1, 1.05$ and 0.95 respectively. Other cosmological parameters assume the standard values.	75
5.3	The marginal distributions of the free parameters, constrained by the three-year WMAP data. In addition to the free parameters $\omega_b \equiv \Omega_b h^2, \omega_c \equiv \Omega_c h^2, H_0, z_{re}, n_s, A_s$ and ρ , shown also are the derived distributions of the density parameter of matter (Ω_m) and cosmological constant (Ω_Λ). The Hubble parameter is allowed to vary in the range from 40 to $100 \text{ km s}^{-1} \text{ Mpc}^{-1}$ (we will suppress this unit afterwards). Here and thereafter, the maxima of the distributions are arbitrarily normalized to 1	76
5.4	The contour marginal distributions of cosmological parameters plotted against ρ . Among the free parameters, H_0 is the most strongly degenerate with ρ	77
5.5	Same as Fig. 5.3, but with H_0 fixed to be 72 . The spread of ρ is much smaller than that in Fig. 5.3.	78
5.6	The derived marginal distributions of $\ln \rho = -\frac{\kappa_4}{2} \sqrt{\frac{n+2}{2n}} (\sigma_{\text{CMB}} - \sigma_0)$ for $40 < H_0 < 100$ (solid line) and $H_0 = 72$ (dashed line) respectively. Note that the latter has much smaller spread.	79

List of Tables

1.1	The values and constraints of various cosmological density parameters from WMAP and SDSS LRG data. Error bars are 1σ .	14
3.1	The constraints on the variation of G at various redshifts. The CMB constraint fills the gap in the “redshift ladder” in between neutron star mass and BBN.	42
5.1	The present constraints on the variation of $\langle H \rangle$ at various redshifts. The CMB constraint fills the gap in the “redshift ladder” in between BBN and quasar. The future Planck data will tighten the CMB constraint (so that it is compatible with other constraints.)	80

Chapter 1

Overview of Cosmology

In this chapter we shall review the current status of cosmology, especially the most important pillars of modern cosmology. Cosmology was once regarded as a data-starved subject. This sentiment can be reflected from Lev Landau's remarks, "*Cosmologists are often wrong but they are never in doubt.*" However, observations have been improving since last couple of decades, and we see the volume and accuracy of the data increasing rapidly. We are now beginning to hear that we are in the era of precision cosmology more and more often. The basic framework of cosmology has been proven to be so robust that it is dubbed the standard model of cosmology. This is a brief review on the standard Λ CDM model; for more details the reader may consult cosmology textbooks [6, 7, 8] or lecture notes [9, 10].

1.1 Friedmann-Robertson-Walker Universe

Today every competent cosmologist accepts the Big Bang paradigm without much doubt. The idea that the universe originates from a hot expanding "fireball" is in good agreement with three cosmological observations: the Hubble diagram, the Cosmic Microwave Background Radiation and the Big Bang Nucleosynthesis. To make the description of the Big Bang more precise, we now

introduce the Robertson-Walker (RW) metric

$$ds^2 = -dt^2 + a^2(t) \left[\frac{dr^2}{1 - kr^2} + r^2(d\theta^2 + \sin^2\theta d\phi^2) \right], \quad (1.1)$$

where k is the curvature, and $a(t)$ is the scale factor. The RW metric can be derived [9] from the cosmological principle, which states that the universe is homogeneous and isotropic at every point. This principle is required to establish a scientific theory of the universe and is due to our modesty that we are not living in a special point in the universe. Recent observations (see Fig. 1.4 and 1.6) strengthen our confidence in this principle.

In Eq. 1.1, k describes the curvature of the spatial slices and can be normalized to +1, 0 or -1 for positive, zero and negative spatial curvature respectively. Note that the RW metric is due to geometry and is not dependent on the details of general relativity (GR). But to determine the evolution of $a(t)$ we do need the Einstein field equation:

$$R_{\mu\nu} - \frac{1}{2}Rg_{\mu\nu} + \Lambda g_{\mu\nu} = 8\pi GT_{\mu\nu}. \quad (1.2)$$

Here we explicitly include the cosmological constant Λ and $T_{\mu\nu}$ is the energy-momentum tensor. In cosmology it is often sufficient to model the energy-momentum tensor as a perfect fluid

$$T_{\mu\nu} = (\rho + p)U_\mu U_\nu + pg_{\mu\nu}, \quad (1.3)$$

where ρ and p are density and isotropic pressure measured in the rest frame of the perfect fluid, whose 4-velocity is U^μ . Plugging Eq. 1.1 and 1.3 into Eq. 1.2, we yield the Friedmann equation

$$\left(\frac{\dot{a}}{a}\right)^2 = \frac{8\pi G}{3}\rho - \frac{k}{a^2} + \frac{\Lambda}{3} \quad (1.4)$$

and the acceleration equation

$$\frac{\ddot{a}}{a} = -\frac{4\pi G(\rho + 3p)}{3} + \frac{\Lambda}{3}. \quad (1.5)$$

From Eq. 1.4 and Eq. 1.5, we can derive the continuity equation

$$\dot{\rho} = -3\frac{\dot{a}}{a}(\rho + 3p). \quad (1.6)$$

To characterize the property of each component, we can define the equation of state (EOS) as

$$w \equiv \frac{p}{\rho}. \quad (1.7)$$

Often but not always w is assumed to be constant. Given w , by Eq. 1.6, the cosmological density scales as

$$\rho \propto \frac{1}{a^{3(w+1)}}. \quad (1.8)$$

With the scaling laws of the densities, Eq. 1.4 is sufficient to determine the evolution of the $a(t)$.

1.2 The Hubble Diagram and Type Ia Supernovae

The strongest evidence of the expansion of the universe is the Hubble diagram. First, we have to introduce the Hubble parameter

$$H \equiv \frac{\dot{a}}{a}. \quad (1.9)$$

It is a measure of the expansion rate of the universe.

In 1929, Edwin Hubble observed that the farther the galaxies distance d were the greater the velocities v that they receded from us. He further concluded the Hubble law

$$v = H_0 d. \quad (1.10)$$

The value of H_0 measured by Hubble was $500 \text{ km s}^{-1} \text{ Mpc}^{-1}$, wrong by a factor of 7 in hindsight of the current data.

It is easy to get the redshifts by measuring the absorption line spectra of the distant objects. The observed redshift is mainly due to the cosmological redshift z defined as

$$z + 1 \equiv \frac{\lambda_0}{\lambda_e} = \frac{a_0}{a_e}, \quad (1.11)$$

where λ_0 (a_0) denotes the wavelength of a photon (scale factor) at the present time, while λ_e (a_e) represents the wavelength of the photon (scale factor) at the emission time. To a large extent, the wavelength is stretched by the cosmic expansion and the contribution from the Doppler shift is small.

It is much more difficult to get the distance of a heavenly object. One popular approach is to make use of the so-called “standard candles”, whose intrinsic brightness is believed to be known and so their observed brightness can be used as a distance measure. Shown in Fig. 1.1 is a modern Hubble diagram obtained by the Hubble Space Telescope (HST) Team. The modern value of H_0 is $72 \pm 8 \text{ km s}^{-1} \text{ Mpc}^{-1}$ [1].

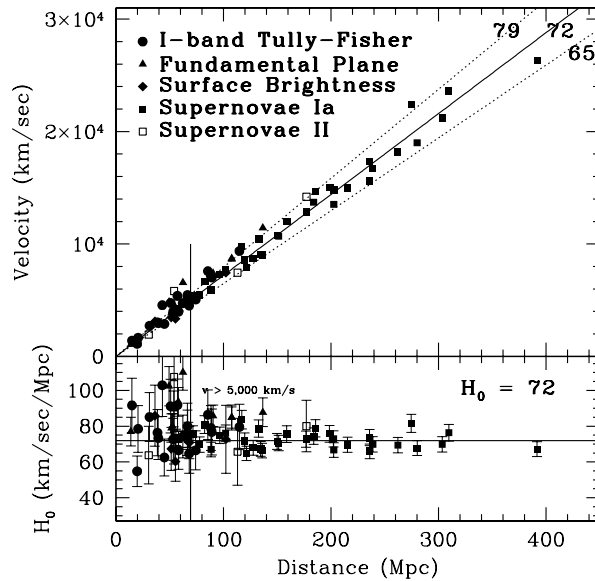


Figure 1.1: Hubble diagram obtained by the HST Key Project [1]. Five different distance measures are used to estimate distance. Relative to other measures SNe Ia extends the observable distance by a factor of 2. They collectively indicate that $H_0 = 72 \pm 8 \text{ km s}^{-1} \text{ Mpc}^{-1}$.

Among the five measures in Fig. 1.1, a type of distance measure Type Ia Supernovae (SNe Ia) stands out and extends the distance to as far as 400 Mpc. A SNe Ia explosion occurs when the infall of mass from a companion star causes the mass of a white dwarf to reach the Chandrasekhar limit. The assumption that SNe Ia are standard candles is based on the universality of the Chandrasekhar limit. A supernova can be as bright as the host galaxy, and so it can be seen even at high redshift. However, the exploding white dwarfs may vary in composition, and the observed peak brightness varies. Nonetheless some corrections have been developed to deal with it.

Not only have the SNe Ia observations sharpened the accuracy of the H_0 , but also given rise to one of the most important (if not the most) discoveries at the end of the last century – that the universe is dominated by a mysterious component called dark energy [11, 12].

The dark energy is a smooth component that becomes dominant in the universe only recently. It has negative pressure so that it drives the recent cosmic acceleration. One of the simplest candidates of dark energy is the cosmological constant Λ . The discovery of cosmic acceleration revives Einstein’s cosmological constant.

1.3 Big Bang Nucleosynthesis

In the early universe, the temperature is so high that particles in the primordial plasma interact strongly with each other. Thus they are in thermal equilibrium. When the universe expands and cools down, the interaction rates of some species of particles cannot catch up with the expansion rate of the universe and they decouple from the rest of the plasma. After falling out of equilibrium, their abundances freeze out. For the equilibrium between the

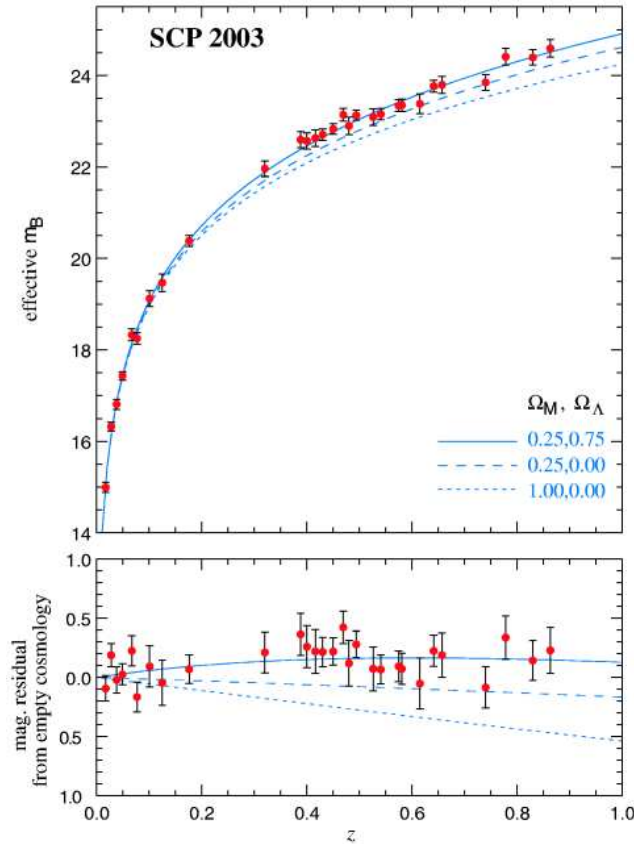


Figure 1.2: Hubble diagram from SCP [2]. In the upper panel, the effective magnitude is plotted against the redshift. The solid curve ($\Omega_\Lambda = 0.75$) fits the data much better than those with $\Omega_\Lambda = 0$. The lower panel shows the residuals relative to an empty universe ($\Omega_\Lambda = 0, \Omega_M = 0$), illustrating how strong the dark energy has been detected.

neutrons and protons, the relevant interactions are the weak interactions

$$n \leftrightarrow p + e^- + \bar{\nu}, \quad (1.12)$$

$$e^+ + n \leftrightarrow p + \bar{\nu}, \quad (1.13)$$

$$\nu + n \leftrightarrow p + e^-. \quad (1.14)$$

This type of interconversion stops when the temperature drops below 1 MeV, a few minutes after the birth of the universe. Since neutron is more massive than proton, the ratio of the freeze-out abundance is about 1/6. The neutron starts to decay with a life time of 890 s. Due to the huge number of photons in the plasma preventing the formation of nuclei, Big Bang Nucleosynthesis

(BBN) is insignificant until the temperature reaches 100 keV. Now the ratio of number density between neutron and proton is about 1/7. Nearly all neutrons are trapped within ${}^4\text{He}$ nuclei because helium is more stable than other light nuclei, while the rest of the protons form hydrogen nuclei. Thus about 25% of baryon mass appears in the form of helium after BBN, while the other 75% in the form of hydrogen. BBN also produces traces of other light nuclei such as deuterium, ${}^3\text{He}$ and lithium. The abundances of ${}^4\text{He}$ and other light elements from theoretical BBN calculations are compared with observational bounds in Fig. 1.3. We see that they are in good agreement with each other.

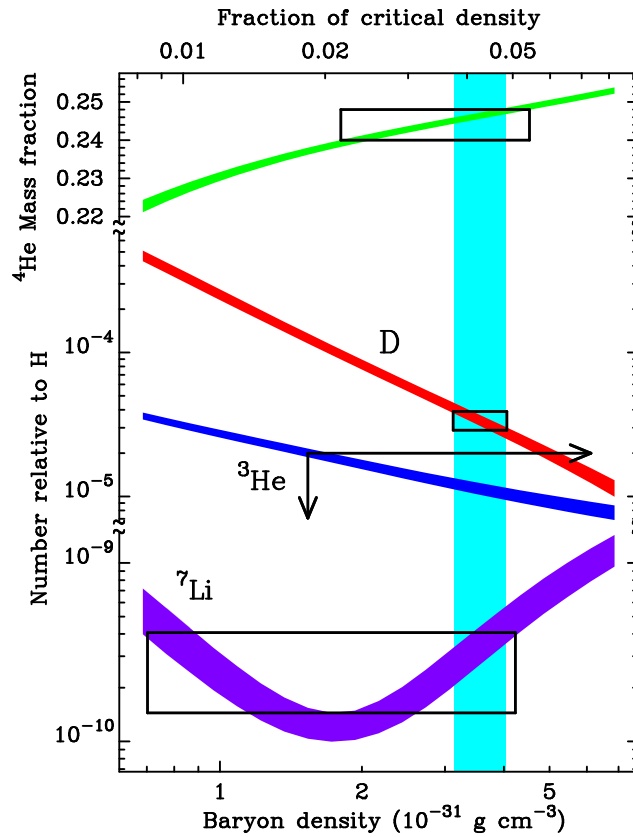


Figure 1.3: The BBN prediction of abundance of ${}^4\text{He}$, deuterium, ${}^3\text{He}$ and ${}^7\text{Li}$ as a function of baryon density. The bands are due to uncertainties in theoretical calculations. The boxes and arrows represent the 95% abundance limits from observations, and the vertical strip indicates the constraints from the measurement of primordial deuterium alone. This figure is taken from Ref. [3].

1.4 Cosmic Microwave Background

A similar decoupling occurs for hydrogen atoms when the universe cools down to the temperature of the order of atomic energy. Before decoupling, Thomson scattering keeps electrons in equilibrium with photons, while protons couple to electrons via Coulombic interactions, and so the hot plasma is in thermal equilibrium. Because of the tight coupling between photons and the plasma, the universe is opaque. About 3.8×10^5 years after the Big Bang, protons recombine with electrons. Once the hydrogen atoms form, the universe becomes transparent to photons and they free-stream through the universe. Nearly free of contaminations in their journey, the primordial photons maintain a blackbody spectrum

$$B_\nu = 2h \frac{\nu^3}{c^2} \frac{1}{e^{h\nu/kT} - 1}. \quad (1.15)$$

Under cosmic expansion, the frequency ν scales with $1/a(t)$, and so the blackbody spectrum can be preserved with $T \propto 1/a(t)$. The temperature is measured to be 2.728 ± 0.004 K [13]. Since the peak frequency is in the microwave range, this primordial radiation is termed Cosmic Microwave Background (CMB) ¹.

More interestingly, since our universe is not perfectly smooth (our existence proves this!), we expect that there are tiny perturbations seeded in the CMB. These anisotropies in the CMB prove to be very difficult to detect. The smallness of the anisotropies in turn confirm the validity of the cosmological principle.

In 1992, CMB anisotropies were first detected by the satellite mission COBE ². Fig. 1.4 shows the CMB anisotropy map measured by the ongoing satellite mission the Wilkinson Microwave Anisotropies Map (WMAP).

¹CMB was detected accidentally by Penzias and Wilson in 1965. They got the Nobel Prize in Physics in 1978

²The 2006 Nobel Prize in physics was awarded to John Mather and George Smoot for their efforts to use COBE to measure the blackbody spectrum and anisotropies of CMB respectively.

The CMB temperature is very uniform on the whole sky, with fluctuations $\delta T/T$ of the order of 10^{-5} only. These fluctuations encode primordial information, and CMB is a powerful weapon to study the physics in the early universe. To compare with theory, the fluctuations in Fig. 1.4 are usually expanded in

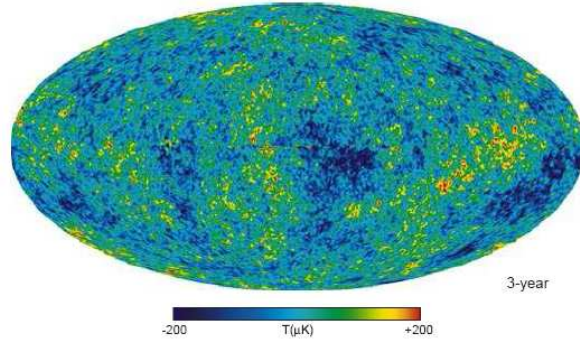


Figure 1.4: The three-year WMAP temperature anisotropy map. Spots are fluctuations in the CMB temperature across the celestial sphere. The magnitude of fluctuations $\delta T/T$ is of the order of 10^{-5} . The figure is taken from [4].

spherical harmonics $Y_{lm}(\theta, \phi)$ as

$$\frac{\delta T}{T} = \sum_{l,m} a_{lm} Y_{lm}(\theta, \phi). \quad (1.16)$$

This operation is similar to Fourier transform except that the basis functions are the spherical harmonics due to the spherical geometry of the celestial sphere. It enables us to separate the small angular scale physics from the large ones. The fluctuations are quantified by the temperature power spectrum

$$C_l = \langle |a_{lm}|^2 \rangle. \quad (1.17)$$

Formally, this is an ensemble average. In practice, since we only observe one universe, it is averaged over the celestial sphere assuming different parts of the sky constitute independent samples.

Shown in Fig. 1.5 is the temperature power spectrum from WMAP and other experiments. The peaks in the temperature power spectrum reveal the oscillations of the primordial acoustic waves. From this spectrum, people have

cranked out a lot of useful information; to name some of the most important ones, the nature of the initial conditions, the spatial curvature, and matter contents of the universe. We shall discuss more about CMB anisotropies in Chapter 2.

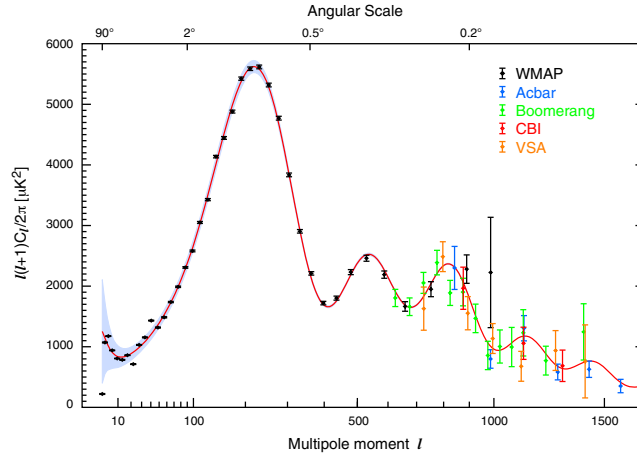


Figure 1.5: The temperature power spectrum from three-year WMAP, together with other ground/balloon experiments dedicated to measuring high- l spectrum. The solid line represents the best fit Λ CDM model. This figure is taken from [4].

1.5 Matter Power Spectrum and Galaxy Surveys

In the standard cosmology picture, initial perturbations grow due to gravitational instability and eventually form large scale structures (LSS), such as galaxies that we see in today's clumpy universe.

In the studies of LSS, we are interested in the density perturbation field

$$\delta(\mathbf{x}) \equiv \frac{\rho(\mathbf{x}) - \langle \rho \rangle}{\langle \rho \rangle}, \quad (1.18)$$

which describes the fluctuation in density at point \mathbf{x} from the mean density $\langle \rho \rangle$. To describe the statistics of $\delta(\mathbf{x})$, we shall consider the two-point correlation function

$$\xi(\mathbf{x}_1, \mathbf{x}_2) \equiv \langle \delta(\mathbf{x}_1)\delta(\mathbf{x}_2) \rangle. \quad (1.19)$$

Again we are taking ensemble average in our mind.

In Fourier space the power spectrum $P(\mathbf{k}_1, \mathbf{k}_2)$ is defined as

$$P(\mathbf{k}_1, \mathbf{k}_2) \equiv \frac{1}{(2\pi)^3} \langle \delta(\mathbf{k}_1) \delta(\mathbf{k}_2) \rangle, \quad (1.20)$$

where $\delta(\mathbf{k})$ is the Fourier transform of $\delta(\mathbf{x})$. Statistical homogeneity and isotropy give

$$P(\mathbf{k}_1, \mathbf{k}_2) = \delta_D(\mathbf{k}_1 - \mathbf{k}_2) P(k_1), \quad (1.21)$$

with

$$P(k_1) = (2\pi)^3 \int \xi(|\mathbf{r}|) e^{i\mathbf{k}\cdot\mathbf{r}}. \quad (1.22)$$

More specifically, the Dirac delta function arises from statistical translation invariance and the fact that $P(\mathbf{k}_1, \mathbf{k}_2)$ is a function of k_1 follows from statistical rotational invariance. The power spectrum is a measure of the spread, or the variance of the density field.

Working in Fourier space is convenient because it enables us to make use of the statistical translation symmetry of the density distribution [10]. The Fourier mode $\delta(\mathbf{k})$ is an eigenmode of the translation operator, and so the cosmic covariance matrix in Eq. 1.20 commutes with the translation operator. In consequence, we have several nice properties: Each Fourier mode $\delta(\mathbf{k})$ grows independently in the linear regime; different modes do not correlate and the covariant matrix Eq.1.20 is diagonal.

Again the reader is reminded that in real surveys the ensemble average is replaced by the volume average. One of the ways to measure the matter power spectrum is to map out the galaxies in the sky. There have been several large galaxy surveys devoted to measuring the matter power spectrum, notably the 2dF Galaxy Redshift Survey (2dFGRS) and the Sloan Digital Sky Survey (SDSS).

Unlike CMB, which is linear and clean, there are two main obstacles in constraining cosmology with galaxy surveys. Ideally, the redshift measured is

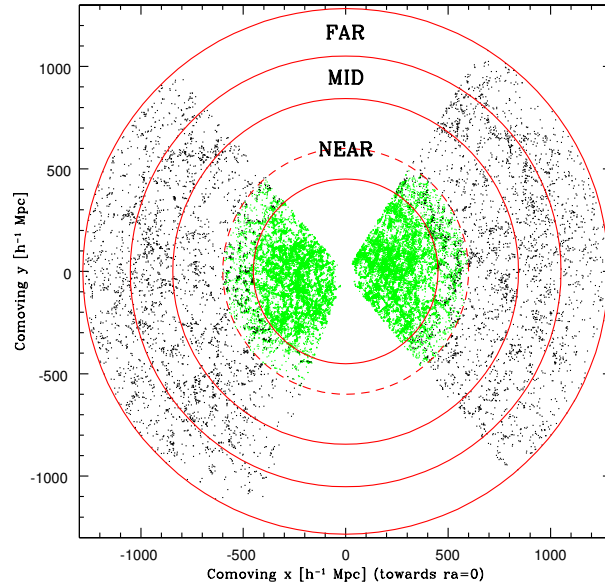


Figure 1.6: The distribution of main galaxies (grey/green) and Luminous Red Galaxies (LRG) in SDSS [5]. These two types of galaxies are singled out from the SDSS dataset for further analysis. The measured LRGs are as far as $z \sim 0.5$. This image of large scale structures provides a glimpse of the primordial fluctuations spectrum and enables us to constrain the cosmological parameters, especially Ω_M .

due to the Hubble flow only, but real galaxies fall into larger structures and have random velocities. This will distort the redshift space, causing systematic deviations in measuring redshift. The second problem arises from the fact that power spectrum of galaxies may not trace the underlying matter power spectrum. The mess of the astrophysics of galaxy formation is summarized by astronomers as a “bias”, b . For simplicity, it is often assumed that b is constant. Nevertheless, there are techniques that have been developed to attack these problems. From the data in Fig. 1.6, the SDSS team derived the matter power spectra, as shown in Fig. 1.7.

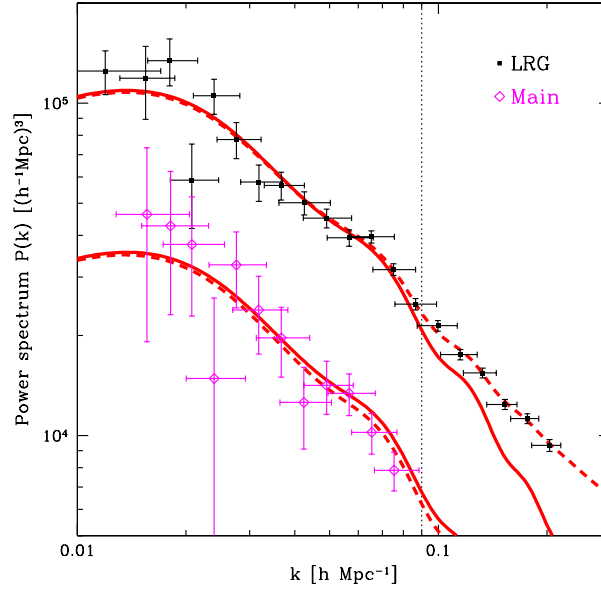


Figure 1.7: Measured power spectra from the LRG and main galaxy samples. The solid lines are the best fit linear Λ CDM models, while the dashed lines include nonlinear corrections. The galaxy bias b are different for these two types of galaxies. This figure is taken from the SDSS collaboration [5].

1.6 The Energy Density Budget of the Universe and Outlook

From the observations that we mentioned and others, we are now able to divide the pie of the contents of the universe with confidence. It is assuring that various observations involving different techniques and underlying physics suggest similar figures.

From Eq.1.4, we see that the spatial curvature k can be determined using the present total density (including Λ) and the Hubble parameter H_0 . It is useful to define the critical density, ρ_{crit} , as

$$\rho_{crit} = \frac{3}{8\pi G} H_0^2. \quad (1.23)$$

The universe is spatially flat if the total density ρ_{tot} is equal to ρ_{crit} , spatially closed if $\rho_{tot} > \rho_{crit}$ and spatially open if $\rho_{tot} < \rho_{crit}$. ρ_{crit} is about 10^{-29} g

cm^{-3} and it turns out that it equals ρ_{tot} .

There are three major components in the universe: baryons, cold dark matter and dark energy. It is convenient to normalize the density of each component with respect to ρ_{crit} , and call it density parameter Ω . In Table 1.1, we show the current values of various density parameters measured from the WMAP and SDSS LRG data [5]. Being able to pin down the values of these parameters is one of the greatest triumphs of modern cosmology.

Parameter	Meaning (normalized w. r. t. ρ_{crit})	Current value
Ω_{tot}	the total density	$1.003^{+0.010}_{-0.009}$
Ω_B	baryon density	$0.0416^{+0.0019}_{-0.0018}$
Ω_C	cold dark matter density	$0.197^{+0.016}_{-0.015}$
Ω_Λ	cosmological constant density	$0.761^{+0.017}_{-0.018}$
Ω_k	spatial curvature	$-0.0030^{+0.0095}_{-0.0102}$
Ω_ν	neutrino density	< 0.024 (95% confidence)

Table 1.1: The values and constraints of various cosmological density parameters from WMAP and SDSS LRG data. Error bars are 1σ .

Besides their numerical values, what are the components really made of? Why do they take on these values? A lot of efforts (and hundreds of papers) have been devoted to addressing these tough questions. Baryons are just the ordinary standard model (SM) particles such as protons and neutrons. But for the dark sector, we really don't know much. Although there are several occasions demanding the existence of dark matter and we have several SM candidates, we don't know exactly what it is (or they are). For the dark energy, it is more intriguing. It surprised everybody when it was found that our universe suffused with a smooth energy density with negative pressure. It is possible that the cosmological constant is due to vacuum fluctuations, but detailed calculations yield a value that differs from the observed one by 120 orders of magnitude. In addition to a plain cosmological constant, there are more exotic ideas such as quintessence, other vacuum energy or modified gravity (see *e.g.* [14, 15, 16]).

Today, the connection between high energy physics and cosmology is very strong because the universe can be a very good testbed for many exotic ideas in high energy physics. As the energy scale in high energy physics increases the theories are hopeless to be tested in accelerators. But it is possible to look for signals from the early hot universe. Formally, the energy scale in cosmology can be extrapolated to as high as the Planck energy scale 10^{19} GeV, beyond which we do not have much physical insight. Thus many high energy physics processes can be realized at least once in the life time of universe. Another advantage of cosmology is that the universe is big. Gravity is much weaker than other forces, and so it is extremely difficult to test gravity in the laboratory without being spoilt by the systematics. However the gravitational force is dominant over cosmological scales. Deviations of unification theories or modified gravity from the standard GR may be constrained cosmologically. The dark sector, especially the dark energy, hardly interacts with the SM particles except gravitationally. Thus it is natural that they are discovered by their gravitational actions in large scales.

The ultimate way to select the good models from so many innovative proposals in cosmology and high energy physics is to confront them with real observational and/or experimental data. By doing so we can eliminate the bad models or reduce the allowed parameter space, so that investigators can concentrate on certain types of promising models or the reduced parameter space. At present we have a large quantity of high accuracy data, and model builders cannot be arbitrary but have to pay a lot of attention to observations. On the other hand, those models that survive the tests from various cosmological constraints certainly deserve our attention.

Realizing that we now have freshly released high precision data from WMAP, we shall mainly make use of CMB anisotropies to constrain some non-standard physics models in this thesis. Given that the perturbations are of the order of 10^{-5} only, linear analysis is sufficient for CMB. The CMB spectra are also

highly Gaussian because the primordial perturbations are Gaussian and the evolution is linear. CMB is also free of many late time contaminations that plague large scale structure surveys. We shall discuss the CMB physics more extensively in Chapter 2.

One of the consequences of physics beyond SM is that the fundamental “constants” may vary. In Chapter 3, we shall look at the CMB constraints on the cosmological variation of gravitational constant G . The CMB constraints will bridge the gap between BBN constraints and many local constraints.

In Chapter 4, we shall constrain a type of modified gravity model, the $f(R)$ gravity, which is attractive because it may explain the recent cosmic acceleration. In addition to CMB data, we will also make use of the SDSS and SNe Ia data because the model we study is expected to deviate from standard GR at late time significantly.

Extra dimension models are hot these days, partly due to the popularity of string theory. The existence of extra dimensions provides a natural framework for variation of constants. We shall investigate and constrain by CMB the induced variation of constants in a brane world model (Chapter 5).

Chapter 2

Review of CMB Physics

In Section 2.1, we shall review the physics and the cosmological information that can be learned from the features of CMB power spectra, such as the peak positions and the relative heights of the peaks. In Section 2.2, we start from the Boltzmann equation to compute the CMB power spectrum.

2.1 Main Physics of the CMB Power Spectra

In this section, we shall follow the treatments in Ref. [17, 18] to discuss the key physics that lead to the formation of acoustic peaks and the cosmological information embedded in the CMB power spectra. For more complete discussions, see [8].

2.1.1 Photon-Baryon Fluid

Before the era of CMB recombination $z_* \sim 1000$, electrons act as glue between photons and baryons with Thomson scattering and Coulomb interaction respectively. We shall model the photon-baryon system as a fluid, which can be described by continuity equations and Euler equations. Because of the tight coupling before recombination, it is a good approximation to consider only the monopole (temperature), Θ , and dipole (velocity), \mathbf{v}_γ , moments of the photon distribution, and monopole (density perturbation), δ_b , and the dipole

(velocity), v_b , moments of the baryon distribution. However, during recombination, the mean free path of photons increases rapidly, and tight coupling approximation is not sufficient to describe the evolution of the perturbations in recombination. Deviations from tight coupling would require higher order multipoles, notably the quadrupole moment of photon distribution, π_γ .

We shall work in the Fourier space because each eigenmode evolves independently in the linear regime. We can restrict ourselves to a single \mathbf{k} mode, and align the z -axis along the \hat{k} direction. Hence the perturbation only excite the $m = 0$ multipoles. In other words, we have azimuthal symmetry for this problem.

In the early universe, we assume that the vector perturbation is small and so we have $\mathbf{v}_\gamma = -iv_\gamma \hat{\mathbf{k}}$ and $\mathbf{v}_b = -iv_b \hat{\mathbf{k}}$.

The effect of gravity comes from the perturbations in the metric. Without perturbations, the metric is simply the FRW metric. In Newtonian gauge, the scalar perturbations to the FRW metric is diagonal. The Newtonian gravitational potential (the time-time metric fluctuation) is $\delta g_{tt} = 2\Psi$, and the spatial curvature fluctuation (space-space metric fluctuation) is $\delta g_{ij} = 2a^2\Phi\delta_{ij}$.

With these notations defined, we can write down the continuity equation for photon temperature

$$3\dot{\Theta} = -kv_\gamma - 3\dot{\Phi}, \quad (2.1)$$

where a dot denotes the derivative with respect to the conformal time η

$$d\eta \equiv \frac{dt}{a(t)}. \quad (2.2)$$

The factor 3 in front of $\dot{\Theta}$ arises because it is the number of photons n_γ , which is proportional to T^3 , that conserves, but not the photon temperature T . The last term appears because the curvature fluctuations Φ perturb the scale factor a , and the photon temperature T is proportional to $1/a$. Therefore a change in Φ induces a change in the temperature fluctuation Θ . Analogously, the

continuity equation for baryons is

$$\dot{\delta}_b = -kv_\gamma - 3\dot{\Phi}. \quad (2.3)$$

This equation states the conservation of baryon number. The last term appears again since perturbation in a due to Φ causes the baryon density to change.

Momentum conservation for photons leads to the Euler equation

$$\dot{v}_\gamma = k\Theta + k\Psi - \frac{k}{6}\pi_\gamma - \dot{\tau}(v_\gamma - v_b), \quad (2.4)$$

with $\dot{\tau}$ the differential scattering cross-section given by

$$\dot{\tau} = an_e\sigma_T, \quad (2.5)$$

where σ_T denotes the Thomson cross-section, and n_e is the electron number density. On the right hand side of Eq. 2.4, $k\Psi$ is the potential gradient, which drives the potential flow. The infall is counteracted by the stress gradients in the fluid. In a perfect fluid, there is an isotropic pressure gradient

$$\begin{aligned} \frac{k\delta p_\gamma}{p_\gamma + \rho_\gamma} &= \frac{k\delta\rho_\gamma}{4\rho_\gamma} \\ &= k\Theta, \end{aligned} \quad (2.6)$$

while in an imperfect fluid, there is an additional anisotropic stress gradient $k\pi$. The coupling term between photons and baryons $\dot{\tau}(v_\gamma - v_b)$ is due to Thomson scattering, which drives the plasma towards homogeneity. There is a similar Euler equation for baryons:

$$\dot{v}_b = -\frac{\dot{a}}{a}v_b + k\Psi + \frac{\dot{\tau}}{R}(v_\gamma - v_b), \quad (2.7)$$

where R is the photon-baryon momentum density ratio

$$R = \frac{\rho_b + p_b}{\rho_\gamma + p_\gamma} \approx \frac{3\rho_b}{4\rho_\gamma}. \quad (2.8)$$

The physical meaning of the term $-\frac{\dot{a}}{a}v_b$ is that the physical momentum decays in an expanding universe and this is called the Hubble drag.

From these continuity equations and Euler equations, we are going to derive an oscillator type equation. First of all, we notice that in scales larger than the photon mean free path $\dot{\tau}^{-1}$, $k/\dot{\tau}$ is a small parameter (or, the optical depth τ is large). Expanding Eq. 2.7 to first order in k/τ , we have

$$v_b = v_\gamma - \frac{R}{\dot{\tau}}(v_\gamma + \frac{\dot{a}}{a}v_\gamma - k\Psi). \quad (2.9)$$

Putting Eq. 2.9 into Eq. 2.4 to eliminate v_b and dropping the π_γ term, we obtain

$$\frac{d}{d\eta} [(1+R)v_\gamma] = k[\Theta + (1+R)\Psi], \quad (2.10)$$

we have made use of $\dot{R} = \frac{\dot{a}}{a}R$.

Finally, combining Eq. 2.10 and Eq. 2.1 yields a forced, damped harmonic oscillator equation

$$\ddot{\Theta} + \frac{\dot{a}}{a} \frac{R}{1+R} \dot{\Theta} + k^2 c_s^2 \Theta = -\frac{k^2}{3} \Psi - \frac{\dot{a}}{a} \frac{R}{1+R} \dot{\Phi} - \ddot{\Phi}, \quad (2.11)$$

where we have defined the sound speed of the photon-baryon fluid, c_s , as

$$c_s^2 \equiv \frac{1}{3(1+R)}. \quad (2.12)$$

The presence of baryons makes the fluid more sluggish. The Newtonian potential Ψ and temporal change of Φ serve as driving forces of the oscillator. So, Eq. 2.11 basically describes the acoustic oscillation caused by the competition between the gravitational driving force and the restoring stress gradients. This oscillation causes compression and rarefaction of the plasma and eventually leads to the cold and hot spots that we observe in the temperature map.

2.1.2 Initial Conditions

To solve Eq. 2.11, we need the initial conditions. The standard picture is that the initial conditions are set by inflation, in which the universe undergoes an exponentially rapid expansion prior to the radiation-dominated era, resulting

in more than 60 e -folds increase in size. In most models, the inflation is driven by a scalar field, called inflaton. Inflation solves the problems why the universe is so flat (the flatness problem) and why the seemingly causally unconnected parts of the universe have the same CMB temperature (the horizon problem). In this paradigm, the quantum fluctuations are magnified by inflation and subsequently form the fluctuations embedded in CMB (so we are quantum mechanical in the sense that we come from quantum fluctuations). These fluctuations provide the initial conditions for acoustic oscillation. Gravitational infall into the potential wells gradually generates the large scale structures in the universe today.

Because an exponential expansion is self-similar in time, the fluctuations are scale-invariant. The energy carried in the fluctuations of the inflaton perturbed the spatial curvature, resulting in slight deviation from perfect flatness in each scale. We have argued previously that curvature perturbations give rise to temperature fluctuations through the perturbation on the scale factor.

In the simplest inflationary models, the stress-energy of the universe is perturbed such that on large scales it can be characterized by a single, spatially uniform EOS, and this type of perturbation is called adiabatic. Inflation sets the phase of the oscillators at different scales in phase. Another popular type of initial conditions, called the isocurvature perturbations, seeks to obey causality and perturb the EOS locally. Such models generally predict the phases of the oscillators to be scale dependent, and this causes the coherent peaks to be washed out. Observation of coherent peaks with a vanishing phase gives a strong support for inflation.

2.1.3 Acoustic Peaks

We now solve Eq. 2.11. To solve it accurately, the algebra would be rather involved and the solution is complicated. It is instructive to consider a matter-dominated universe with negligible baryon content. Thus we can set Φ and Ψ to constant and $R = 0$.

If the oscillator is initially displaced but with negligible velocity, the temperature fluctuation and velocity are given by

$$\begin{aligned} [\Theta + \Psi](k, \eta) &= [\Theta + \Psi](k, 0) \cos(ks), \\ v_\gamma(k, \eta) &= \sqrt{3} [\Theta + \Psi](k, 0) \sin(ks), \end{aligned} \quad (2.13)$$

where s is the sound horizon defined as

$$s \equiv \int_0^\eta c_s d\eta. \quad (2.14)$$

Note that we deliberately write the effective temperature as $\Theta + \Psi$ because it is the observed one. We can understand this by imagining a photon emerging from a hot spot of temperature fluctuation Θ ; it will be redshifted by an amount of Ψ as it climbs out of the potential well. Thus we will see the outgoing photon with temperature $\Theta + \Psi$.

From Eq. 2.13, we see that the temperature at large scales ($ks_* \ll 1$) hardly evolves and the initial condition is preserved; the temperature at the small scales exhibits temporal oscillations due to the competition between pressure gradients and gravity. The smaller is the scale (large k), the larger is the frequency of oscillation. All the oscillations are frozen in at CMB recombination. Let s_* denote the sound horizon at CMB recombination; then the maximum or minimum temperatures are attained when $k_n = n\pi/s_*$. The point is that these extremum temperatures show up as peaks in the CMB temperature power spectrum. Hence we expect to see a series of acoustic peaks corresponding to k_n . The velocity is $\pi/2$ out of phase with the temperature. It does not

generate coherent peaks in the temperature power spectrum. Nonetheless, we shall see that it is the prime mover of the polarization peaks.

The physical scale (k) on the last scattering surface projects to us as angular scale ($1/l$) in the following geometrical way. The symbol l is the order of multipole moment. A spatial inhomogeneity of wavelength λ at the last scattering surface is seen by us today as an angular anisotropy characterized by angle θ roughly by the relation $\theta \sim \frac{D_*}{\lambda}$, where D_* is the angular diameter distance between us and the last scattering surface. In harmonic space, we have a similar relation

$$l_n \approx nl_a, \quad (2.15)$$

with $l_a = \pi D_*/s_*$. In a spatially flat universe, $D(\eta_*) = \eta_0 - \eta_* \approx \eta_0$, where η_0 is the present conformal time. For a non-flat universe,

$$D(\eta_*) = \begin{cases} \mathcal{R} \sin(\frac{d}{\mathcal{R}}) & \text{if } \Omega_k > 0, \\ \mathcal{R} \sinh(\frac{d}{\mathcal{R}}) & \text{if } \Omega_k < 0, \end{cases} \quad (2.16)$$

where d is the coordinate distance, and \mathcal{R} is the radius of curvature $\mathcal{R} = (H_0 \sqrt{|\Omega - 1|})^{-1}$.

Therefore the overall peak positions are sensitive to the spatial curvature of the universe. In particular, we expect the first peak to be located at $l < 220$ for a spatially open universe, while $l > 220$ for a spatially closed one. Measurement of the position of the first peak at $l \approx 220$ is a strong confirmation of the flatness of the universe.

2.1.4 Baryons in Action

In this section we add baryons back to the plasma to see its effects on the acoustic peaks. We consider a matter-dominated universe with a constant yet non-zero R . The solution to the SHO Eq. 2.11 becomes

$$\begin{aligned} [\Theta + \Psi](k, \eta) &= [\Theta + (1 + R)\Psi](k, 0) \cos(ks) - R\Psi(k, 0) \\ &= (1 + 3R)\frac{1}{3}\Psi(k, 0) \cos(ks) - R\Psi(k, 0), \end{aligned} \quad (2.17)$$

where we have used, in the last line, $\Theta + \Psi = \frac{\Psi}{3}$, the Sachs-Wolfe effect, in a matter-dominated universe. Besides slowing down the sound speed by Eq. 2.12, the baryons also increase the amplitude of oscillation by a factor of $1 + 3R$ and shift the equilibrium point of oscillations. The shift of the equilibrium position by an amount of $-R\Psi(k, 0)$ breaks the symmetry between odd and even peaks. In the standard model, the baryons increase the power of odd peaks and suppress the power of even ones. Therefore, by observing the heights of the odd peaks and even peaks the abundance of baryons can be constrained.

2.1.5 Damping

The baryon-photon fluid has slight imperfections due to shear viscosity and heat conduction. These two effects have been included in Eq. 2.4 and 2.7 by the anisotropic stress term π_γ and momentum exchange term $\dot{\tau}(v_\gamma - v_b)$. When the optical depth is large in the sense that $k/\dot{\tau} \gg 1$, the fluid is isotropic in the rest frame and heat conduction is negligible. The presence of the imperfections damps the acoustic oscillations.

The viscosity term is proportional to the quadrupole moment, which is caused by the velocity gradient kv_γ , while the anisotropic stress is eliminated by scatterings, the effectiveness of which is characterized by $\dot{\tau}$. Hence $\pi_\gamma \propto kv_\gamma/\dot{\tau}$. Using Eq. 2.1 $kv_\gamma \approx -3\dot{\Theta}$, we see that viscosity gives rise to a damping term in the harmonic oscillator equation. Heat conduction terms can be shown to yield a similar term in the equation. Therefore, we expect that there is an extra damping factor of the order $\exp(-\frac{k^2\eta}{\dot{\tau}})$ in the solution of damped oscillator equation. Hence we can define a characteristic damping scale k_d :

$$k_d = \sqrt{\frac{\dot{\tau}}{\eta}}, \quad (2.18)$$

which is the reciprocal of the geometric mean of the Hubble horizon η and the photon mean free path $\dot{\tau}^{-1}$. The damping effect can be visualized as

random walk of photons between hot spots and cold spots, through which the distinct temperature anisotropies are blurred. Thus we expect damping to be most serious for the small scales and the high order multipoles are washed out. Indeed, numerical calculations give $k_d s_* \approx 10$, and so the peaks beyond the third peak are substantially suppressed, which also agrees with current observations.

2.1.6 Polarization

The Thomson scattering of photons off an electron can generate polarization. The differential scattering cross-section is given by

$$\frac{d\sigma}{d\Omega} = \frac{3\sigma_T}{8} |\hat{k}_i \cdot \hat{k}_s|^2, \quad (2.19)$$

where \hat{k}_i and \hat{k}_s denote the incident and outgoing photon directions respectively.

However, it can be shown that if photons incident in the distributions of monopole and dipole towards an electron, the scattered radiation is unpolarized. We need the quadrupole of the photon distribution to give net linear polarization. Furthermore, Thomson scattering cannot produce circular polarization. Quadrupole is of the order $kv_\gamma/\dot{\tau}$, and so we expect the polarization to be down by a factor of $k/\dot{\tau}(\eta_*)$. Polarization is generated during CMB recombination because polarization formation needs both anisotropies and free electrons. Prior to CMB recombination, scattering quickly wipes out the anisotropies; after CMB decoupling, there are no free electrons as scatterers. Numerical calculations show that the power of CMB polarization is about 10% of its temperature counterpart.

Polarization is a “headless vector”, and so it is unchanged upon rotation of the coordinate system by 180° . CMB polarization is usually described in terms of E and B modes, which are scalars and have definite parity under inversion. In the linear theory, scalar perturbations generate E -mode polarization only.

In contrast to peaks in the temperature power spectrum, whose primary source is monopole of the photon distribution, the peaks in polarization power spectrum are due to v_γ . Recall that in Eq. 2.13, v_γ is out of phase with Θ ; this is the reason why the temperature power spectrum is also out of phase with the polarization. Because of the phase relation, polarization is correlated with temperature. The temperature-polarization power spectrum C_l^{TE} exhibits twice the acoustic frequency because $C_l^{TE} \sim \sin(ks_*) \cos(ks_*)$.

CMB polarization can be used as a consistency check because it can be constructed once the temperature power spectrum is obtained. Polarization is also useful to break the degeneracy between some of the cosmological parameters. Finally, it allows us to probe the last scattering surface directly because it is mostly affected by the physics during CMB recombination.

2.2 Computation of CMB Power Spectrum

We will illustrate how the CMB power spectrum is computed from the Boltzmann equation. Unlike in previous section, we will consider the temperature perturbation, Δ_T instead of just the first few moments. The roadmap is that we first derive the so-called line-of-sight integral solution, which is an integral of the product of perturbations and some exponential functions over the conformal time (line-of-sight). We then integrate over all the k modes to get the total perturbations. From the photon perturbation, we can compute the power spectrum. We shall see that the tight coupling solutions, *i.e.*, the monopole, dipole and quadrupole free stream to form high order multipoles because of the geometric projection. Mathematically, the transformation is realized through the intermediary spherical Bessel function j_l . We shall demonstrate the procedures with temperature perturbation. For polarization, the procedure is similar and one may refer to [19].

We will denote the direction of line-of-sight (or the photon direction) \hat{n} and

the direction of perturbation \hat{k} is chosen to be parallel to the z -axis. The direction cosine $\hat{n} \cdot \hat{k}$ is denoted by μ . The full Boltzmann equations for temperature perturbation $\Delta_T(k, \eta, \mu)$ and polarization perturbation $\Delta_P(k, \eta, \mu)$ are

$$\dot{\Delta}_T + ik\mu\Delta_T = -ik\mu\Psi - \dot{\Phi} + \dot{\tau} \left[-\Delta_T + \Delta_{T0} - i\mu v_b - \frac{1}{2}P_2(\mu)\Pi \right] \quad (2.20)$$

$$\dot{\Delta}_P + ik\mu\Delta_P = \dot{\tau} \left[-\Delta_P + \frac{1}{2}P_2(\mu)\Pi \right], \quad (2.21)$$

$$\Pi = \Delta_{T2} + \Delta_{P0} + \Delta_{P2}, \quad (2.22)$$

where $P_l(\mu)$ is the l th Legendre polynomial.

We want to find the line-of-sight integral solution to Eq. 2.20. First, move $\dot{\tau}\Delta_T$ to the left hand side and multiply both sides by the integrating factor $e^{ik\mu\eta-\tau}$, where

$$\tau(\eta) \equiv \int_{\eta}^{\eta_0} d\eta' \dot{\tau}(\eta'). \quad (2.23)$$

After a little bit of manipulations, Eq. 2.20 becomes

$$\frac{d}{d\eta} (e^{ik\mu\eta-\tau} \Delta_T) = e^{ik\mu\eta-\tau} \tilde{S}, \quad (2.24)$$

where for simplicity we have defined

$$\tilde{S} \equiv -ik\mu\Psi - \dot{\Phi} + \dot{\tau} \left[\Delta_{T0} - i\mu v_b - \frac{1}{2}P_2(\mu)\Pi \right]. \quad (2.25)$$

Integrating, we have

$$\Delta_T(k, \eta_0, \mu) = e^{-ik\mu\eta_0} \int_0^{\eta_0} d\eta e^{ik\mu\eta-\tau} \tilde{S}, \quad (2.26)$$

where we have used, by definition Eq. 2.23, $\tau(\eta_0) = 0$, and the fact that $\tau(0)$ is basically infinite. It is desirable to separate the geometry (μ) from the “source” (\tilde{S}). In fact this can be done using integration by parts. Let’s illustrate with a function $A(\eta, \mu)$:

$$\begin{aligned} \int_0^{\eta_0} d\eta e^{ik\mu(\eta-\eta_0)} e^{-\tau} A(\eta, \mu) &= \frac{1}{ik\mu} \left[e^{ik\mu(\eta-\eta_0)} e^{-\tau} A(\eta, \mu) \Big|_0^{\eta_0} \right. \\ &\quad \left. - \int_0^{\eta_0} d\eta e^{ik\mu(\eta-\eta_0)} \frac{d}{d\eta} (e^{-\tau} A(\eta, \mu)) \right]. \end{aligned} \quad (2.27)$$

Note that the surface term at $\eta = 0$ is zero. For the surface term at η_0 , as \tilde{S} is quadratic, it would contribute to the monopole and dipole in the power spectrum, but they are irrelevant because the monopole term contributes to an overall temperature, and the dipole term is interfered by our own orbital velocity. Thus we can discard the surface terms. The rule is to replace each μ in \tilde{S} by

$$\mu \rightarrow -\frac{1}{ik} \frac{d}{d\eta}. \quad (2.28)$$

Therefore we now have

$$\Delta_T(k, \eta_0, \mu) = \int_0^{\eta_0} d\eta e^{ik\mu(\eta-\eta_0)} S(k, \eta), \quad (2.29)$$

with the source function S

$$\begin{aligned} S(k, \eta) \equiv & (\dot{\Psi} - \dot{\Phi})e^{-\tau} + \left(\Delta_{T0} + \frac{v_B}{k} + \Psi + \frac{1}{4}\Pi + \frac{3}{4k^2}\ddot{\Pi} \right) g \\ & + \left(\frac{v_b}{k} + \frac{3}{2k^2}\dot{\Pi} \right) \dot{g} + \frac{3}{4k^2}\Pi\ddot{g}, \end{aligned} \quad (2.30)$$

where we have defined the visibility function

$$g(\eta) \equiv \dot{\tau} e^{-\tau}. \quad (2.31)$$

This function is sharply peaked about the last scattering surface; it can be interpreted as the probability density that a photon is last scattered at η .

Now we are in a position to sum over all the \mathbf{k} modes to get the total scalar contribution to the temperature perturbation. The temperature perturbation in the direction \hat{n} is

$$\frac{\delta T}{T}(\hat{n}) = \int d^3\mathbf{k} \xi(\mathbf{k}) \Delta_T(k, \eta, \mu), \quad (2.32)$$

where $\xi(\mathbf{k})$ is the primordial density perturbation field satisfying

$$\langle \xi^*(\mathbf{k}_1) \xi(\mathbf{k}_2) \rangle = P(k_1) \delta(\mathbf{k}_1 - \mathbf{k}_2), \quad (2.33)$$

where $P(k_1)$ is the primordial power spectrum.

Recall that the temperature power spectrum is defined as

$$C_l^{TT} = \frac{1}{2l+1} \sum_m \langle a_{Tlm}^* a_{Tlm} \rangle, \quad (2.34)$$

where a_{Tlm} is given by

$$a_{Tlm} = \int d\Omega Y_{lm}^*(\hat{n}) \frac{\delta T}{T}(\hat{n}). \quad (2.35)$$

Putting Eq. 2.35 into Eq. 2.34 and making use of Eq. 2.32, we get

$$C_l^{TT} = \frac{1}{2l+1} \int d^3\mathbf{k} P(k) \sum_m \left| \int d\Omega Y_{lm}^*(\hat{n}) \Delta_T(\tau_0, k, \mu) \right|^2. \quad (2.36)$$

Substituting Δ_T by Eq. 2.29, and noticing that

$$\int d\Omega Y_{lm}^*(\hat{n}) e^{-ik(\eta-\eta_0)} = \sqrt{4\pi(2l+1)} (-i)^l j_l [k(\eta_0 - \eta)] \delta_{m0}, \quad (2.37)$$

we finally have

$$C_l^{TT} = (4\pi)^2 \int dk k^2 P(k) \left[\int_0^{\eta_0} S(k, \eta) j_l [k(\eta_0 - \eta)]^2 \right]. \quad (2.38)$$

In fact the integral inside the square bracket is the l th order moment of the the perturbation $\Delta_T(k, \eta_0)$. C_l^{TT} is the temperature power spectrum that we seek.

The power spectrum C_l^{TT} completely characterizes the covariance matrix of a_{Tlm} by the relation

$$\langle a_{Tl'm'}^* a_{Tlm} \rangle = C_l^{TT} \delta_{ll'} \delta_{mm'}. \quad (2.39)$$

Chapter 3

Constraints on Variation of the Gravitational Constant by CMB

We make use of the CMB power spectra to constrain the cosmological variation of Newtonian gravitational constant G in this Chapter. The variation of G is modeled by a step function and a linear function of scale factor a respectively. It is found that the sensitivity of CMB to the variation of G is enhanced when we require G to converge to its present value. This Chapter is organized as follows. In Section 3.1, we describe the current constraints on variation of G and the theories that provide a natural platform for G to vary. Our parametrizations for the variation of G are given in Section 3.2. The effects of variation of G on the CMB power spectra are investigated in Section 3.3. In Section 3.4, we study the constraints on the variation of G by the three-year WMAP data using the method of Markov Chain Monte Carlo (MCMC) and discuss the results obtained. Section 3.5 is devoted to the conclusion. This Chapter is very similar to our paper published in Phys. Rev. D ¹ [20].

¹K. C. Chan and M.-C. Chu, Phys. Rev. D **75**, 083521 (2007)

3.1 Current Constraints on G and Theoretical Motivations

One of the fundamental questions in physics is whether the fundamental constants are truly constant. Indeed the possibility of cosmological variation of “constants” has long been proposed [21]. Among the fundamental constants, the gravitational constant G is the least accurately measured. The value of G is measured in the laboratory and applied to all scales. To check for the constancy of G , tests should be done at different spatial and temporal scales. There are many tests at redshifts of order 0. For example, the lunar laser ranging experiment, which monitors the distance between the earth and the moon by laser ranging technique, can be used to put a bound on the variation of G [22]. If G varies during the history of the earth, the surface temperature and size of the earth would change. However the earth does not preserve a good record of the gravitational conditions. Increase in G causes the Sun to burn at a faster rate, and the depth of the convective zone is affected, which can be observed in the vibrational modes of the Sun, in particular the p mode [23]. Since an increase in G also shortens the life spans of stars, the ages of stars in globular clusters can be used to put a constraint on the deviation of G from its present value [24]. Because the Chandrasekhar mass $M_{Ch} \propto G^{-3/2} m_N^{-2}$ sets the mass scale of neutron stars, by observing the masses of neutron stars formed at different redshifts, limits on G in the past 10 Gyr or so have been derived in [25]. The highest redshift, of about 10^{10} , constraint comes from Big Bang Nucleosynthesis (BBN). An increase in the expansion rate during the epoch of BBN causes the freeze-out to occur earlier, and the abundances of neutron and hence ${}^4\text{He}$ are enriched [26]. For details of various experiments and observations, see the review article by Uzan [27] (see also [28]).

On the theory side, there have been grand unification theories and string/M theory motivated models predicting that some of the fundamental “constants”,

such as the fine structure constant α and the Newtonian gravitational constant G , may vary over time. In theories with extra dimensions, the effective gravitational constant in 4D spacetime depends on the more fundamental mass scale in the bulk and the size of the extra dimensions [29]. If the size of the extra dimensions evolves over time, the effective constants in 4D will vary as well. For example, the DGP model [30] has been put forward to explain the recent observation that the universe is in an accelerating phase without invoking the dark energy. It was argued that the acceleration is due to the leakage of gravity into the extra dimensions.

3.2 Parametrization of G

To select promising ones from the myriads of models in the literature, one may constrain possible variations of the fundamental “constants” using observational data. There have been efforts trying to constrain the possible variation of G using cosmological data. In particular, since the Cosmic Microwave Background Anisotropies is sensitive to many cosmological parameters, it could be used to constrain the variation of G . CMB is unique because it offers a long look back time. The physics of CMB is particularly clean as it involves only well known physics in the linear regime. One approach is to constrain the variation of G in some particular types of models, *e.g.* the CMB spectra in the Brans-Dicke cosmology are discussed in Ref. [31, 32]. However, given the multiplicity of models in the literature, it seems more practical to use a simple and generic parametrization for G . In [33, 34], the authors have used the CMB power spectra to constrain the possible variation of G with a parameter λ as

$$G = \lambda^2 G_0, \quad (3.1)$$

where G_0 is the present laboratory-measured value. It was assumed that λ is a constant over the age of the universe (and only suddenly becomes 1 at the

present time). However this assumption is unrealistic since we know that G should converge to its present value to avoid conflicts with other experiments and observations. We shall call the convergence of G to its present value *stabilization*. One can imagine that G may vary in many different manners over the history of the universe, and so it is hopeless to deal with all possibilities one by one. In this Chapter we study two generic stabilization schemes. One of them is instantaneous stabilization. That is we consider an abrupt gravitational transition and model the variation of G by a step function:

$$\lambda^2 = \begin{cases} \lambda_0^2 & \text{if } a < a_s, \\ 1 & \text{if } a \geq a_s, \end{cases} \quad (3.2)$$

where a is the scale factor and a_s is the scale factor at which stabilization occurs. Another is that G varies smoothly and we parametrize it as a linear function of a :

$$\lambda^2 = \begin{cases} \lambda_0^2 & \text{if } a < a_*, \\ 1 - \frac{a_s - a}{a_s - a_*} (1 - \lambda_0^2) & \text{if } a_* \leq a \leq a_s, \\ 1 & \text{if } a > a_s, \end{cases} \quad (3.3)$$

where a_* is the scale factor at the time of photon decoupling. Our main goal is to constrain the range of λ_0^2 in Eq. 3.2 and Eq. 3.3. We assume that the underlying mechanism for the variation of G does not affect other physics so that the standard CMB calculation with the modifications of Eq. 3.1- 3.3 is valid. The Friedmann equation is modified as

$$\left(\frac{\dot{a}}{a^2} \right)^2 = \lambda^2(a) H^2(a), \quad (3.4)$$

with

$$H^2(a) = H_0^2 \left(\frac{\Omega_M}{a^3} + \frac{\Omega_\gamma}{a^4} + \Omega_\Lambda \right), \quad (3.5)$$

where a dot denotes derivative with respect to the conformal time, H_0 is the present Hubble parameter, Ω_M is the density parameter of the non-relativistic

matter, Ω_γ is the density parameter of radiation, and Ω_Λ is the density parameter of the cosmological constant. Note that we consider a flat universe here.

3.3 Effect of Variation of G on the CMB Temperature and Polarization Power Spectra

It has been pointed out in Ref. [33] that the CMB angular power spectrum does not change using the simple prescription Eq. 3.1 as far as the dynamical equations are concerned. The ratio between the sound horizon and the distance to the last scattering surface (LSS), Θ , will not change if both are blown up by the same factor due to the varied gravitational constant in the flat universe. However, the scaling is not perfect since the recombination physics does introduce another scale. The recombination is dictated mainly by the binding energy of hydrogen atom, which is not affected by a change in the gravitational constant. If the expansion rate is greater during the epoch of recombination, it will be more difficult for the protons and electrons to recombine, and the ionization fraction x_e will increase. Recall that the probability density that a photon last scatters at a conformal time η is given by the visibility function [17],

$$g(\eta) = \dot{\tau} e^{-\tau}, \quad (3.6)$$

with

$$\dot{\tau} = an_e \sigma_T, \quad (3.7)$$

where n_e is the number density of electrons and σ_T is the Thomson cross-section. The increase in x_e broadens $g(\eta)$, resulting in more severe damping of the high l peaks. However the duration that the photons stay in contact with the LSS is also shortened as the expansion rate is greater. Because the two effects partially cancel each other, the damping is not increased much even

when G is increased by a large amount. In Fig. 3.1, we show the temperature power spectra for $\lambda_0^2 = 0.5$ and 3 compared to the unchanged one ($\lambda_0^2 = 1$) for the case of instantaneous stabilization with the stabilization redshift $z_s \equiv \frac{1}{a_s} - 1 = 0$. A large change in G is required for noticeable changes in the spectra. The damping effect can be partially compensated by reionization, and so the details of reionization such as the degree of reionization affect the sensitivity of the spectra to λ .

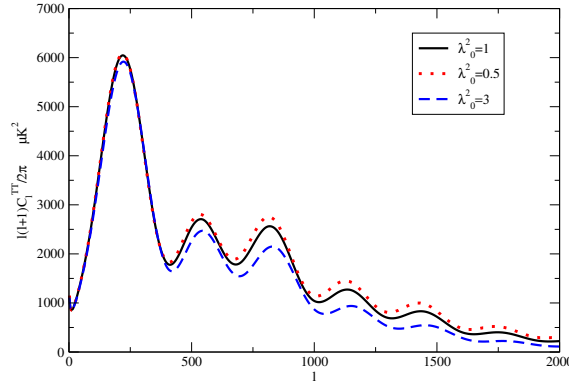


Figure 3.1: The CMB temperature angular power spectra for three values of the Newtonian gravitational constant with instantaneous stabilization $z_s = 0$. The solid, dotted and dashed curves correspond to $\lambda_0^2 = 1, 0.5$ and 3 respectively. The damping effect is only noticeable for $l > 500$.

The above conclusion that the CMB angular power spectrum is not sensitive to the value of G is based on the assumption that the gravitational constant remains different from the present laboratory-measured-value till “yesterday.” However G must converge to its present value so that there is no conflict with the low-redshift constraints. When G changes as described in Eq. 3.2 or Eq. 3.3, the expansion history of the universe is modified, the fractional change in the sound horizon at the epoch of decoupling is different from that in the conformal distance to the LSS, and the resultant CMB spectra will be distorted. Fig. 3.2 shows the temperature power spectra with instantaneous stabilization at $z_s = 0$ and 10. Note that the “standard” spectrum ($\lambda_0^2 = 1$

and $z_s = 0$) nearly coincides with the one for $\lambda_0^2 = 1.2$ and $z_s = 0$. If, however, the stabilization redshift is at $z_s = 10$, the spectrum for $\lambda_0^2=1.2$ (0.8) shifts to larger (smaller) l scales. In fact, it is conceptually simpler to compare the one for $\lambda_0^2 = 1.2$, $z_s = 0$ to the one with $\lambda_0^2 = 1.2$ and $z_s = 10$. The size of the sound horizon is the same for both cases while the distance to the LSS is increased for $z_s = 10$; as a result Θ becomes smaller and the spectrum shifts to high l scales. The same argument applies to the one with $\lambda_0^2 = 0.8$ and $z_s = 10$, but with the opposite effect. Because of the dramatic gravitational transition, we observe an enhanced late Integrated Sachs Wolfe (ISW) effect in the small l scales.

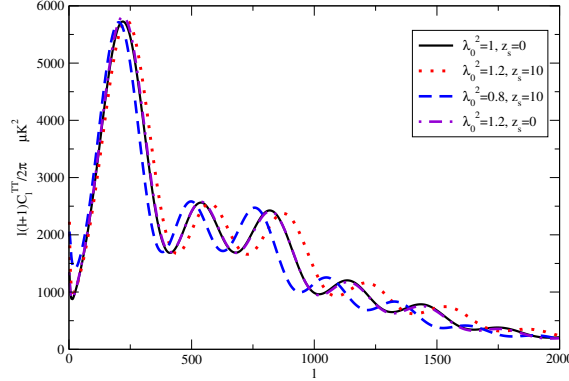


Figure 3.2: Same as Fig. 3.1 but with spectra with $z_s = 10$ in contrast with those with $z_s = 0$. The standard spectrum (solid) nearly coincides with the one with $\lambda_0^2 = 1.2$ and $z_s = 0$ (dot-dashed). When instantaneous stabilization occurs at $z_s = 10$, marked shifts to larger (smaller) l scales result for $\lambda_0^2 = 1.2$ (dotted) (0.8 (dashed)).

We observe similar sideway shifts in the E-type polarization and TE cross polarization spectra as well. In Fig. 3.3, we show the E-polarization power spectra with instantaneous stabilization at $z_s = 0$ and 10. In Ref. [33], the authors proposed that the degeneracy between the expansion rate and the scalar spectral index n_s can be lifted by measuring the polarization, because the formation of polarization is proportional to the width of the visibility

function. An increase in G causes the power of the polarization spectrum to increase in small l scales and then decrease in large l scales. But the effect of stabilization is much more appreciable.

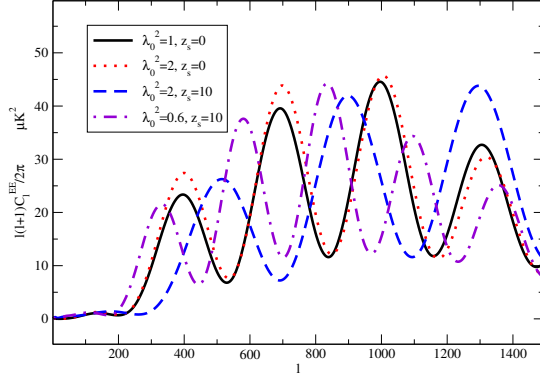


Figure 3.3: The E-polarization spectra with instantaneous stabilization at $z_s = 0$ and 10. The peaks shift to larger (smaller) l scales for $\lambda_0^2 = 2$ (0.6) when instantaneous stabilization takes place at $z_s = 10$, in contrast to the cases without stabilization ($z_s = 0$).

When G varies linearly with a , its effects on the CMB power spectra are still dominated by the sideways shifts discussed in the instantaneous stabilization scenario, as can be seen in Fig. 3.4. The effects are qualitatively similar for the two stabilization schemes that we use.

Since our prescription is simple, we can easily estimate the amount of shift in the CMB spectrum due to stabilization. This calculation is similar to that of the CMB shift parameter [35]. From Eq. 3.4, we have the conformal distance to the LSS

$$d_* \equiv \eta_0 - \eta_* = \int_{a_*}^1 \frac{da}{a^2 \lambda(a) H(a)}, \quad (3.8)$$

where η_0 is the present conformal time, and η_* is the conformal time at CMB decoupling. One immediately sees that if λ_0 is larger, the conformal distance will be smaller. This is reasonable because it takes less time for the universe

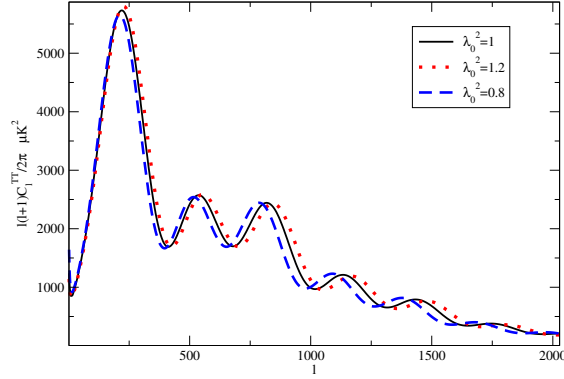


Figure 3.4: The effects of linear variation of G on the temperature power spectrum. The solid line shows the spectrum when there is no variation of G . When $\lambda_0^2 = 1.2$ (0.8), the peaks shift to larger (smaller) l scales. a_s is set to be 1.

to expand to its present size. The peak positions in the CMB temperature angular power spectrum in a flat universe can be characterized by [17]

$$l_n \approx n\pi \frac{d_*}{r_s}, \quad (3.9)$$

where r_s is the sound horizon:

$$r_s = \int_0^{\eta_*} c_s d\eta. \quad (3.10)$$

The sound speed c_s is given by

$$c_s^2 = \frac{1}{3(1+R)}, \quad (3.11)$$

with

$$R = \frac{3\rho_B}{4\rho_\gamma}, \quad (3.12)$$

where ρ_B and ρ_γ are mass densities of baryons and radiations respectively. It should be pointed out that the sound horizon also depends on λ through η . Hence if $\lambda_0 > 1$ at the epoch of CMB decoupling, the size of the sound horizon will also be smaller. In fact, the reduction rates for d_* and r_s are the same if there is no stabilization; the effects of λ are exactly cancelled, a manifestation

that the peaks do not shift if there is no stabilization. However, when there is stabilization, two different scales will be introduced and the peak positions will shift.

We now illustrate with the case of instantaneous stabilization. The calculations can be simplified by noting that if there is no stabilization, the peaks do not shift even if $\lambda_0^2 \neq 1$. The sound horizon is the same irrespective of stabilization if it takes place after decoupling. Hence we only need to compare the conformal distance between the case with stabilization and the one without it:

$$\delta d_* = d_{*NS} - d_{*S} \quad (3.13)$$

$$= \int_{a_s}^1 \left(\frac{1}{\lambda_0} - 1 \right) \frac{da}{a^2 H(a)}, \quad (3.14)$$

where the subscript $_{NS}$ denotes no stabilization and $_{S}$ denotes with stabilization. From Eq. 3.9, the shifts in the peak positions due to the change in G are given by

$$\delta l_n = \frac{n\pi}{r_s} \delta d_*. \quad (3.15)$$

Plugging in the standard Λ CDM model parameters, we have

$$\delta l_n \sim 508n(\lambda_0 - 1)(0.558 - \sqrt{0.311a_s}). \quad (3.16)$$

One may proceed similarly for linear variation of G , but it is too cumbersome to write down the results explicitly. We display $\delta l_n/n = \pi\delta(d_*/r_s)$ against λ_0^2 in Fig. 3.5. We see that the shift in l from the simple arguments here agrees with the full numerical calculations in Fig. 3.2 and Fig. 3.4. Furthermore, the curve by the simplified formula in Eq. 3.16 tracks closely the one from complete calculations of r_s and d_* .

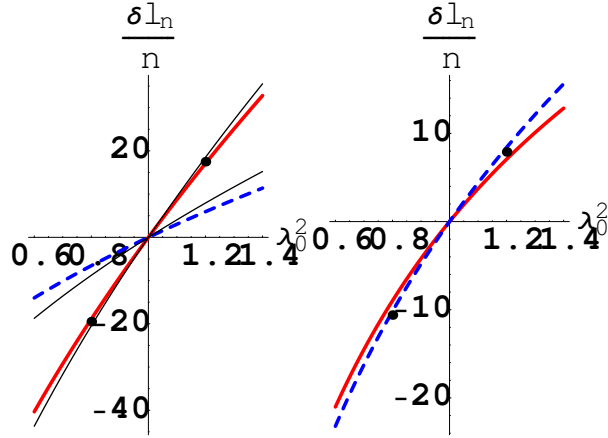


Figure 3.5: The left (right) panel shows $\delta l_n/n = \pi\delta(d_*/r_s)$ vs. λ_0^2 for instantaneous (linear) stabilization. For the plot on the left, the thick (red) solid curve corresponds to $a_s=0.1$ and the dashed curve to $a_s=0.5$. The dots correspond to $\delta l_n/n$ averaged over the first three peaks of the spectra in Fig. 3.2 ($\lambda_0^2 = 1.2, z_s = 10$ and $\lambda_0^2 = 0.8, z_s = 10$). The two thin solid (black) curves are obtained using the simplified formula Eq. 3.16 for $a_s = 1$ and 0.5 respectively. On the right, the solid and dashed curves correspond to linear stabilization with $a_s = 1$ and 0.5 respectively. Similarly we denote by the dots the average $\delta l_n/n$ in Fig. 3.4 for $a_s = 1$, and $\lambda_0^2=1.2$ and 0.8 respectively.

3.4 Constraining G by MCMC and Discussions

Because the CMB angular power spectra are sensitive to various parameters, to be consistent, other relevant parameters should also be varied when fitting with data. A popular means is to make use of the Markov Chain Monte Carlo (MCMC) method (see Appendix A for introduction). With the temperature and polarization spectra computed by the Boltzmann code CMBFAST [36], we employ the public MCMC engine CosmoMC [37] to explore the parameter space. Since the Hubble parameter H_0 is measured to rather good precision by the HST key project, we take $H_0 = 72$ [1]. The constraints we get are not sensitive to this restriction. Thus the free parameters that we vary are: $\omega_B = \Omega_B h^2$, $\omega_{CDM} = \Omega_{CDM} h^2$, z_{re} , the reionization redshift, n_s , the index of the primordial perturbation spectrum, A_s , the normalization amplitude, λ_0^2 , and the stabilization redshift z_s . We use the three year WMAP data [4, 38] to

constrain these parameters.

First of all, we do not consider stabilization; that is, we assume that $z_s = 0$. Imposing the prior that $\lambda_0^2 < 2.2$, we get the constraint on λ_0^2 to be $[0.91, 2.20]$ at 95% confidence level. The bounds seem to be sensitive to the prior on G . The weak constraint on G is expected given the small change in the CMB power spectra even for relatively large variations in G as discussed in Section 3.3. Now we implement the instantaneous stabilization parametrized by Eq. 3.2. Since there are already tight constraints on the variation of G at redshifts of order 0, we impose the prior of $\ln z_s > 0$. On the other hand, we want to constrain the variation of G after CMB decoupling, and thus we impose the prior that $\ln z_s < 6.8$. The marginal distributions of λ_0^2 and $\ln z_s$ are shown in Fig. 3.6. The 2σ confidence intervals of λ_0^2 and $\ln z_s$ are $[0.95, 1.05]$ and $[0, 5.57]$ respectively. With stabilization, the confidence interval of λ_0^2 shrinks substantially. In Fig. 3.7, we show the contour plot of the joint marginal distribution of λ_0^2 and $\ln z_s$. The triangular shape of the distribution is due to the fact that the constraint on λ_0^2 is tighter if $\ln z_s$ is larger.

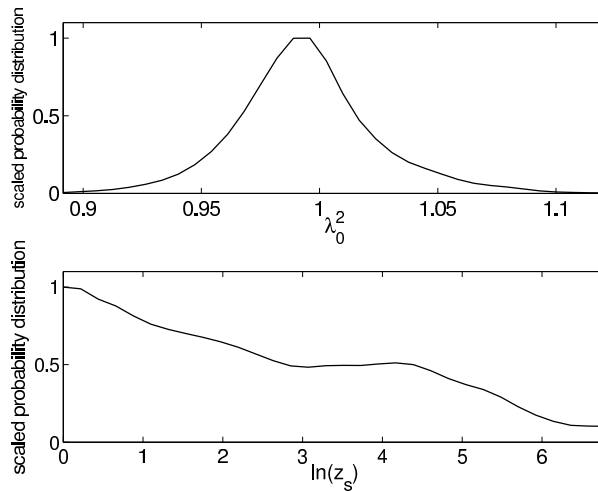


Figure 3.6: The marginal distributions of λ_0^2 and $\ln z_s$ obtained using the three-year WMAP data set in the instantaneous stabilization scenario. Here and thereafter, the maximum of the distribution is normalized arbitrarily to 1.

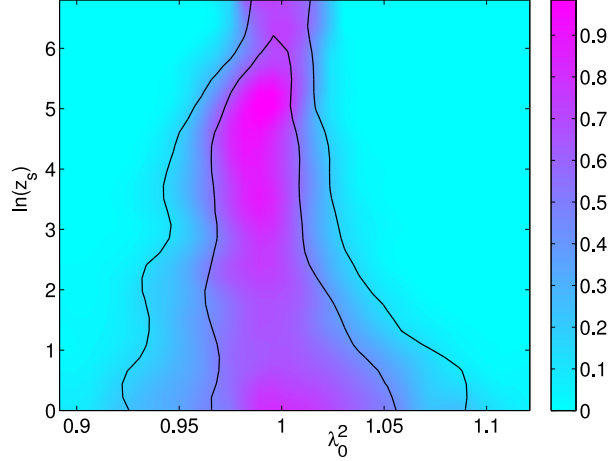


Figure 3.7: The contour plot of the joint distribution of λ_0^2 and $\ln z_s$ constrained using the three-year WMAP data set in the instantaneous stabilization scenario. The inner and outer solid lines are the 68% and 95% confidence level contours respectively.

We now turn to the linear stabilization given in Eq. 3.3. For smooth variation, we set $z_s = 0$. The marginal distribution of λ_0^2 for $z_s = 0$ is shown in Fig. 3.8, and the resultant 95% confidence interval of λ_0^2 is $[0.89, 1.13]$.

Translating the above constraint on the linear parametrization of G to the common form \dot{G}/G , we get $\dot{G}/G = (-9.6 \sim +8.1) \times 10^{-12} \text{ yr}^{-1}$. This is complementary to the constraints from neutron star mass and BBN, which constrain the variation of G in the regimes of redshifts $0 \sim 4$ and 10^{10} respectively [28]. The results are summarized in Table 3.1. We see that the CMB

	redshift	$\dot{G}/G \text{ yr}^{-1}$
Lunar laser ranging [22]	0	$(1 \pm 8) \times 10^{-12}$
Neutron star mass [25]	$0 \sim 4$	$(-0.6 \pm 2.0) \times 10^{-12}$
CMB (WMAP)	$0 \sim 1000$	$(-9.6 \sim 8.1) \times 10^{-12}$
BBN [26]	10^{10}	$(-2.7 \sim 2.1) \times 10^{-11}$

Table 3.1: The constraints on the variation of G at various redshifts. The CMB constraint fills the gap in the “redshift ladder” in between neutron star mass and BBN.

power spectra can extend the constraint on the variation of G to a large range of redshifts that other experiments and observations cannot reach. Improving

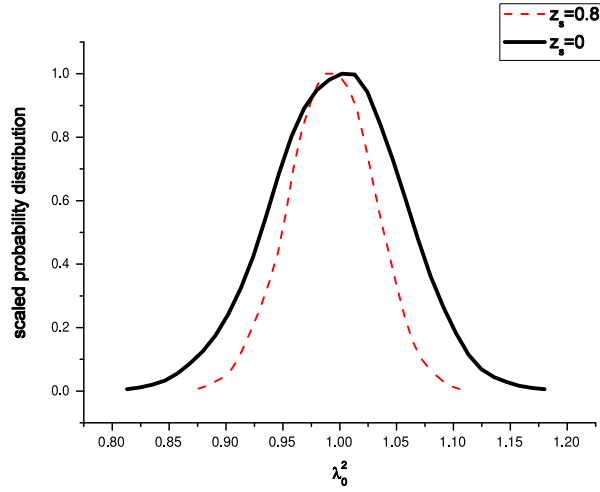


Figure 3.8: The marginal distributions of λ_0^2 for the linear stabilization scenario in Eq. 3.3 with $z_s = 0$ and $z_s = 0.8$ respectively, constraint using the three-year WMAP data.

the low-redshift bounds on G helps to tighten the bounds at high redshifts because we can set z_s to a large value. This is supported in Fig. 3.7 for instantaneous stabilization and also for linear stabilization in Fig. 3.8, where we also plot the marginal distribution of λ_0^2 with $z_s = 0.8$. The allowed range of λ_0^2 is smaller than that of $z_s = 0$.

Although we only consider two types of parametrizations, they in fact encompass a large class of models in which G varies monotonically after photon decoupling. If G varies sharply near some redshift z_s , this can be approximated by the parametrization Eq. 3.2, and the contour distribution in Fig. 3.7 can be applied. On the other hand if G varies in a smooth manner, the linear parametrization Eq. 3.3 can be a good approximation.

We note that other cosmological parameters that we also vary agree well with the standard Λ CDM cosmological parameters given in [39], and so we do not bother to write them down. Without stabilization, all cosmological parameters are still within 2σ from those in the WMAP paper. The agreement gets better when we take stabilization into account. In these cases, all are within 1σ .

From the MCMC runs, we can analyze the degeneracy between λ_0^2 and other cosmological parameters. We see that λ_0^2 has some degeneracy with ω_B , ω_{CDM} and n_s . The degeneracy with ω_B and ω_{CDM} can be understood by the fact that λ_0^2 and ω_i ($i = B$ or CDM) appear in the Friedmann equation as the product $\lambda_0^2 \omega_i$. The change in relative amplitudes on different scales due to λ_0^2 can be compensated by changing the relative amplitudes in the primordial perturbations characterized by n_s [33]. As mentioned earlier, for instantaneous stabilization, λ_0^2 is quite strongly degenerate with $\ln z_s$. It is well-known that the effect of curvature on the spectrum is to shift it sideways, somewhat similar to the effect of stabilization of G , which is the most important contribution to our constraints. Thus we expect that our bounds on λ_0^2 will be weakened by the inclusion of curvature in the fitting.

Since the upcoming Planck satellite mission is going to probe the temperature power spectrum to as high as $l \sim 2500$ and the E-polarization spectrum to $l \sim 1500$, we expect that there will be tremendous improvement in the constraint on λ_0^2 . We can forecast the improvement that Planck will bring us quantitatively using the Fisher matrix, which has been widely used to predict the expected uncertainties in future experiments (see *e.g.* [33, 40] or Appendix B). Under the assumption of Gaussian perturbations and Gaussian noise, the Fisher matrix takes the form

$$F_{ij} = \sum_l \sum_{X,Y} \frac{\partial C_{Xl}}{\partial p_i} (\text{Cov}_{lXY})^{-1} \frac{\partial C_{Yl}}{\partial p_j}, \quad (3.17)$$

where p_i is the i th free parameter and C_{Xl} is the l th multipole of the observed spectrum of type X , which can be the temperature, temperature-polarization and E-polarization spectra. The experimental precision is encoded in the covariant matrix Cov_{lXY} . We find that with the temperature power spectrum alone the current constraint is improved by a factor of 8; when the polarization spectrum is included, the bounds will be tightened by a factor of 11 relatively to our current bounds. The CMB constraints on \dot{G}/G will be potentially one

of the best constraints. Furthermore, it is possible to strengthen the constraint by including the matter power spectrum as well since enhanced ISW effects are induced by the gravitational stabilization.

Finally, we would like to comment on our assumption that G varies homogeneously in the whole universe. In Ref. [41], Mota *et al.* consider the possibility of gravity being spatially inhomogeneous. Using exact solutions in the scalar-tensor theory, they model the gravity inside the inhomogeneity as a small spatially closed universe and match the boundary conditions with the background solution. They find that, due to nonlinearity, the gravitational constant inside the overdense region departs from the background one. According to their results, G in our cluster is likely to be different from the background one. Since analysis of CMB is in the linear regime, the G it constrains is the cosmological one. In the inhomogeneous gravity scenario, since there is no reason that the cosmological G should converge to our local one, our constraints will be relaxed.

3.5 Conclusion

Previously, CMB was used to constrain the variation of G without considering stabilization. Not only are the resultant limits weak, but also this assumption does not respect many tight local constraints. In this work we consider two simple and generic parametrizations of G , the instantaneous stabilization and linear stabilization. Stabilization causes appreciable sideways shifts in the CMB power spectra, and hence the sensitivity of CMB to the variation of G is enhanced. We use the three-year WMAP data to constrain the model parameter(s) and other cosmological parameters. For the case of instantaneous stabilization, we simultaneously constrain λ_0^2 and $\ln z_s$ to $[0.89, 1.13]$ and $[0, 5.57]$ to 2σ intervals. For the linear stabilization scenario, z_s is set to 0 and we get the 95% confidence interval $[0.89, 1.13]$, which is equivalent to

$\dot{G}/G = (-9.6 \sim 8.1) \times 10^{-12} \text{ yr}^{-1}$. Although we only concentrate on two types of parametrization, our results can be applied to a large class of models in which G varies monotonically after CMB decoupling because the variation of G in many of these models can be approximated by either a step function or a linear function. The constraint derived from CMB extends the bounds on G up to the redshift of about 1000, and so it is complementary to other experiments and observations. In particular, it fills the “redshift gap” between BBN and the neutron star mass constraints. With the forthcoming Planck data, the constraints will be improved by a factor of 10 or so, and the constraints on \dot{G}/G from CMB may be one of the best ones.

Chapter 4

Constraints on $f(R)$ Cosmology in the Palatini Formalism

In the general relativity (GR), the metric g_{ab} is the only fundamental dynamical field; yet in some alternative gravitation theories, both the metric and the connection Γ are independent dynamical fields. This approach is called the Palatini formalism. The Palatini formalism yield the standard GR as the metric approach if the Lagrangian density is a linear function of the Ricci scalar R . However, *a priori* the Lagrangian density can be a nonlinear function of R , denoted by $f(R)$.

In this Chapter we make use of the gauge invariant perturbation equations in general theories of $f(R)$ gravity in the Palatini formalism to linear order and calculate the cosmic microwave background (CMB) and matter power spectra for an extensively discussed model, $f(R) = R + \alpha(-R)^\beta$, which is a possible candidate for the late-time cosmic accelerating expansion found recently. These spectra are discussed and found to be sensitively dependent on the value of β . We are thus able to make stringent constraints on β from cosmological data on CMB and matter power spectra: The three-year Wilkinson Microwave Anisotropy Probe (WMAP) data alone gives a constraint $|\beta| \lesssim \mathcal{O}(10^{-3})$ while the joint WMAP, Supernova Legacy Survey (SNLS) and Sloan Digital Sky

Survey (SDSS) data sets tightens this to $\beta \sim \mathcal{O}(10^{-6})$, about an order of magnitude more stringent than the constraint from SDSS data alone, which makes this model practically indistinguishable from the standard Λ CDM paradigm.

The Chapter is organized as follows. Sec. 4.1 is the introduction. In Sec. 4.2, we will first review briefly the theory of $f(R)$ gravity in the Palatini formalism, and we then present the perturbation equations. Then in Sec. 4.3 the CMB and matter power spectra for different choices of parameters are displayed and discussed, and the constraints from various data sets will be presented. Finally, we conclude in Sec. 4.4. Throughout this work we will assume a flat universe filled with cold dark matter, photons, baryons, electrons and 3 species of neutrinos (all massless), that is there is no dark energy. The unit $c = 1$ is adopted, and the metric convention used in this Chapter is $(+, -, -, -)$. This Chapter closely resembles our paper ¹ [42].

4.1 Introduction

It is observed that the universe is now undergoing accelerating expansion [43, 12, 44], which is also consistent with the three-year Wilkinson Microwave Anisotropy Probe (WMAP) data and several other cosmological observations. The usual “explanation” for this involves a mysterious component, called the dark energy, which drives this accelerating expansion. However, this dark energy problem could also be attacked by modifying the theory of gravity so that it departs from the standard general relativity (GR) when the spacetime curvature becomes small. In one type of modified gravity theories, the Ricci scalar R in the Einstein-Hilbert action is simply replaced by a function of R , commonly known as $f(R)$. Indeed, in [45, 46], it was shown that by adding correction terms, such as R^2 , $R^{ab}R_{ab}$ and $R^{abcd}R_{abcd}$, to the action, the late time accelerating cosmic expansion could be reproduced (see also [47] and references therein

¹B. Li, K. C. Chan and M.-C Chu, astro-ph/0610794

for related works). Another argument in favor of such generalizations is that the effective Lagrangian of the gravitational field generally will include higher order terms in the curvature invariants as a result of quantum corrections (see, *e.g.*, [48]).

However, the conventional metric approach to $f(R)$ gravity leads to fourth order equations which may exhibit violent instabilities when matter is present in the weak gravity regime [49] (see however [50] for a discussion). On the other hand, in the Palatini variation of the action where the metric and connection are treated as independent dynamical variables [51], the resultant equations are second order, which are more tractable and concordant with field equations in other branches of physics. In particular, the typical form $f(R) = R + \alpha(-R)^\beta$ has been discussed extensively in the literature as an alternative dark energy model which fits rather well with the supernovae (SNe) Ia data, and it is also tested using cosmic microwave background (CMB) shift parameter and baryon acoustic oscillation (BAO) in [52, 53, 54, 55]. Possible constraints on other types of Palatini- $f(R)$ model have also been considered using big bang nucleosynthesis (BBN) and the requirements that the success of the inflationary paradigm is not spoiled [56]. Recently constraint from data on matter power spectrum alone is given in [57]. As far as we know, there have been no attempts to confront Palatini $f(R)$ gravity models with CMB data to date.

In this work, we will concentrate on the model of $f(R) = R + \alpha(-R)^\beta$, where α is positive (so that it can reproduce the recent cosmic acceleration). We refer to it as the *late* $f(R)$ cosmological model because its corrections to GR dominate very lately, and we study *both* its CMB *and* matter power spectra. For this, we need the perturbation equations in the Palatini formalism, one set of which has been worked out in [58]. Here, however, we will derive a set of covariant and gauge invariant perturbation equations by the method of $3 + 1$ decomposition (see Sec. 4.2) for our calculations. Also we shall try to

constrain the model parameters. Unlike previous works, we use the full three-year WMAP data set [4, 38] instead of the CMB shift parameter only. This $f(R)$ gravity model will be constrained firstly by the WMAP CMB spectra data, and then jointly by the CMB spectra, SNe measurements from Supernova Legacy Survey (SNLS), plus the matter power spectrum data measured by the Sloan Digital Sky Survey (SDSS) [59].

4.2 Field Equations in Theories of Palatini - $f(R)$ Gravity

In this section we shall first summarize the properties of the general theory of $f(R)$ gravity in the Palatini formalism. For more detail introduction, see *e.g.* [60]. We then list its perturbation equations, which have been rederive in [61].

4.2.1 General Theory of $f(R)$ Gravity in the Palatini Approach

The starting point of our discussion on the Palatini- $f(R)$ gravity is the modified Einstein-Hilbert action, which is given as

$$S = \int d^4x \sqrt{-g} \left[\frac{1}{2\kappa} f(R) + \mathcal{L}_m \right], \quad (4.1)$$

where $\kappa = 8\pi G$ (G is the Newton's constant) and $R = g^{ab} R_{ab}(\bar{\Gamma})$ ($a, b = 0, 1, 2, 3$) with $R_{ab}(\bar{\Gamma})$ being defined as

$$R_{ab} \equiv \bar{\Gamma}_{ab,c}^c - \bar{\Gamma}_{ac,b}^c + \bar{\Gamma}_{cd}^c \bar{\Gamma}_{ab}^d - \bar{\Gamma}_{ad}^c \bar{\Gamma}_{cb}^d. \quad (4.2)$$

Notice that the connection $\bar{\Gamma}$ here is not the conventional Levi-Civita connection of the metric g_{ab} , which we shall denote by Γ ; rather it will be treated as an independent field in the Palatini approach to the $f(R)$ theory of gravity. Correspondingly, the tensor R_{ab} and scalar R are also not the Ricci tensor and

Ricci scalar calculated from g_{ab} as in GR, which instead are denoted by \mathcal{R}_{ab} and \mathcal{R} respectively in this work ($\mathcal{R} = g^{ab}\mathcal{R}_{ab}$). The matter Lagrangian density \mathcal{L}_m , on the other hand, is assumed to be independent of $\bar{\Gamma}$, which is the same as in GR.

The extremization of the action Eq. (4.1) with respect to the metric g_{ab} then gives the modified Einstein equations

$$FR_{ab} - \frac{1}{2}g_{ab}f(R) = \kappa\mathcal{T}_{ab}, \quad (4.3)$$

in which $F = F(R) \equiv \partial f(R)/\partial R$ and \mathcal{T}_{ab} is the energy-momentum tensor in the system discussed. The trace of Eq. (4.3) reads

$$FR - 2f = \kappa\mathcal{T} \quad (4.4)$$

with $\mathcal{T} = \rho - 3p$ (ρ is the energy density and p the isotropic pressure) being the trace of the energy-momentum tensor. This is the so-called structural equation [62] which relates R directly to the energy components in the universe: given a specific form of $f(R)$ and thus $F(R)$, R can be obtained as a function of \mathcal{T} by numerically or analytically solving this equation.

The variation of Eq. (4.1) with respect to the connection field $\bar{\Gamma}$ leads to another equation

$$\nabla_a[F(R)\sqrt{-g}g^{bc}] = 0, \quad (4.5)$$

which indicates that the connection $\bar{\Gamma}$ is compatible with a metric γ_{ab} that is conformal to g_{ab} :

$$\gamma_{ab} = F(R)g_{ab}. \quad (4.6)$$

With the aid of Eq. (4.6) we could now easily obtain the relation between R_{ab} and \mathcal{R}_{ab} as

$$R_{ab} = \mathcal{R}_{ab} + \frac{3\mathcal{D}_a F \mathcal{D}_b F}{2F^2} - \frac{\mathcal{D}_a \mathcal{D}_b F}{F} - \frac{g_{ab} \mathcal{D}^c \mathcal{D}_c F}{2F}. \quad (4.7)$$

Note that in above we are using \mathcal{D} and ∇ to denote the covariant derivative operators which are compatible with g_{ab} and γ_{ab} respectively.

Since \mathcal{L}_m depends only on g_{ab} (and, of course, some matter fields) and the energy-momentum conservation law holds with respect to it, we shall treat this metric as the physical one. Consequently the difference between $f(R)$ gravity and GR could be understood as a change in the manner in which the spacetime curvature and thus the physical Ricci tensor \mathcal{R}_{ab} responds to the distribution of matter (through the modified Einstein equations). In order to make this point explicit, we can rewrite Eq. (4.3) by the use of Eq. (4.7) as

$$\begin{aligned} \kappa \mathcal{T}_{ab} &= F \mathcal{R}_{ab} - \frac{1}{2} g_{ab} f \\ &\quad + \frac{3}{2F} \mathcal{D}_a F \mathcal{D}_b F - \mathcal{D}_a \mathcal{D}_b F - \frac{1}{2} g_{ab} \mathcal{D}^c \mathcal{D}_c F, \end{aligned} \quad (4.8)$$

in which $F(\mathcal{T}), f(\mathcal{T})$ are now simply functions of \mathcal{T} .

4.2.2 The Perturbation Equations

The perturbation equations in general theories of $f(R)$ gravity have been derived in [58]. However, here we adopt a different, covariant and gauge invariant derivation which utilizes the method of 3 + 1 decomposition [63, 64, 65].

The main idea of 3+1 decomposition is to make space-time splits of physical quantities with respect to the 4-velocity u^a of an observer. A projection tensor h_{ab} is then defined as $h_{ab} = g_{ab} - u_a u_b$ which could be used to obtain covariant tensors orthogonal to u . For example, the covariant spatial derivative $\hat{\mathcal{D}}$ of an arbitrary tensor field $T_{d\dots e}^{b\dots c}$ (which, by definition, is orthogonal to u) is given as

$$\hat{\mathcal{D}}^a T_{d\dots e}^{b\dots c} \equiv h_i^a h_j^b \dots h_k^c h_d^r \dots h_e^s \mathcal{D}^i T_{r\dots s}^{j\dots k}. \quad (4.9)$$

The energy-momentum tensor and covariant derivative of the 4-velocity u could be decomposed respectively as

$$\mathcal{T}_{ab} = \pi_{ab} + 2q_{(a} u_{b)} + \rho u_a u_b - p h_{ab}, \quad (4.10)$$

$$\mathcal{D}_a u_b = \sigma_{ab} + \varpi_{ab} + \frac{1}{3} \theta h_{ab} + u_a A_b. \quad (4.11)$$

In the above π_{ab} is the projected symmetric trace free (PSTF) anisotropic stress, q the vector heat flux, σ_{ab} the PSTF shear tensor, $\varpi_{ab} = \hat{\mathcal{D}}_{[a}u_{b]}$, $\theta = \mathcal{D}^a u_a = 3\dot{a}/a$ (a is the cosmic scale factor) the expansion scalar and $A_a = \dot{u}_a$ the acceleration. The overdot expressed as $\dot{\phi} = u^a \mathcal{D}_a \phi$ is the derivative with respect to the proper time of the comoving observer moving at velocity u , and the square brackets denote antisymmetrization and parentheses symmetrization. The normalization is chosen to be $u^2 = 1$ in consistence with our metric convention.

Decomposing the Riemann tensor and making use of the modified Einstein equations with the general techniques used in GR, we obtain, after linearization, five constraint equations

$$0 = \hat{\mathcal{D}}^c (\epsilon^{ab}{}_{cd} u^d \varpi_{ab}); \quad (4.12)$$

$$\begin{aligned} \frac{1}{F} \kappa q_a &= \frac{3\dot{F} \hat{\mathcal{D}}_a F}{2F^2} + \frac{\theta \hat{\mathcal{D}}_a F}{3F} - \frac{\hat{\mathcal{D}}_a \dot{F}}{F} \\ &\quad - \frac{2}{3} \hat{\mathcal{D}}_a \theta + \hat{\mathcal{D}}^b \sigma_{ab} + \hat{\mathcal{D}}^b \varpi_{ab}; \end{aligned} \quad (4.13)$$

$$\mathcal{B}_{ab} = \left[\hat{\mathcal{D}}^c \sigma_{d(a} + \hat{\mathcal{D}}^c \varpi_{d(a)} \right] \epsilon_{b)ec}{}^d u^e; \quad (4.14)$$

$$\begin{aligned} \hat{\mathcal{D}}^b \mathcal{E}_{ab} &= \frac{1}{2F} \kappa \left[\hat{\mathcal{D}}^b \pi_{ab} + \left(\frac{2}{3} \theta + \frac{\dot{F}}{F} \right) q_a + \frac{2}{3} \hat{\mathcal{D}}_a \rho \right] \\ &\quad - \frac{1}{2F^2} \kappa (\rho + p) \hat{\mathcal{D}}_a F; \end{aligned} \quad (4.15)$$

$$\hat{\mathcal{D}}^b \mathcal{B}_{ab} = \frac{1}{2F} \kappa \left[\hat{\mathcal{D}}_c q_d + (\rho + p) \varpi_{cd} \right] \epsilon_{ab}{}^{cd} u^b. \quad (4.16)$$

Here ϵ_{abcd} is the covariant permutation tensor, \mathcal{E}_{ab} and \mathcal{B}_{ab} are respectively the electric and magnetic parts of the Weyl tensor \mathcal{W}_{abcd} , given respectively by $\mathcal{E}_{ab} = u^c u^d \mathcal{W}_{acbd}$ and $\mathcal{B}_{ab} = -\frac{1}{2} u^c u^d \epsilon_{ac}{}^{ef} \mathcal{W}_{efbd}$.

We also obtain seven propagation equations:

$$\dot{\rho} + (\rho + p)\theta + \hat{\mathcal{D}}^a q_a = 0; \quad (4.17)$$

$$\dot{q}_a + \frac{4}{3}\theta q_a + (\rho + p)A_a - \hat{\mathcal{D}}_a p + \hat{\mathcal{D}}^b \pi_{ab} = 0; \quad (4.18)$$

$$\begin{aligned} & \dot{\theta} + \frac{1}{3} \left[\theta + \frac{3\dot{F}}{2F} \right] \theta - \hat{\mathcal{D}}^a A_a \\ & - \left[\frac{3\dot{F}^2}{2F^2} - \frac{3\ddot{F}}{2F} - \frac{\kappa\rho}{F} - \frac{f}{2F} - \frac{\hat{\mathcal{D}}^2 F}{2F} \right] = 0; \end{aligned} \quad (4.19)$$

$$\begin{aligned} & \dot{\sigma}_{ab} + \frac{2}{3} \left[\theta + \frac{3\dot{F}}{4F} \right] \sigma_{ab} - \hat{\mathcal{D}}_{\langle a} A_{b \rangle} \\ & + \mathcal{E}_{ab} + \frac{1}{2F} \kappa \pi_{ab} + \frac{1}{2F} \hat{\mathcal{D}}_{\langle a} \hat{\mathcal{D}}_{b \rangle} F = 0; \end{aligned} \quad (4.20)$$

$$\dot{\varpi} + \frac{2}{3}\theta\varpi - \hat{\mathcal{D}}_{[a} A_{b]} = 0; \quad (4.21)$$

$$\begin{aligned} & \frac{1}{2F} \kappa \left[\dot{\pi}_{ab} + \left(\frac{1}{3}\theta - \frac{3\dot{F}}{2F} \right) \pi_{ab} \right] \\ & - \frac{1}{2F} \kappa \left[(\rho + p)\sigma_{ab} + \hat{\mathcal{D}}_{\langle a} q_{b \rangle} \right] \\ & - \left[\dot{\mathcal{E}}_{ab} + \left(\theta + \frac{\dot{F}}{2F} \right) \mathcal{E}_{ab} - \hat{\mathcal{D}}^c \mathcal{B}_{d(a} \epsilon_{b)ec}{}^d u^e \right] = 0; \end{aligned} \quad (4.22)$$

$$\begin{aligned} & \dot{\mathcal{B}}_{ab} + \left(\theta + \frac{\dot{F}}{2F} \right) \mathcal{B}_{ab} + \hat{\mathcal{D}}^c \mathcal{E}_{d(a} \epsilon_{b)ec}{}^d u^e \\ & + \frac{1}{2F} \kappa \hat{\mathcal{D}}^c \pi_{d(a} \epsilon_{b)ec}{}^d u^e = 0, \end{aligned} \quad (4.23)$$

The angle brackets mean taking the trace free part of a quantity.

Besides the above equations, it would also be useful to express the projected Ricci scalar $\hat{\mathcal{R}}$ in the hypersurfaces orthogonal to u^a (the projected Riemann tensor, $\hat{\mathcal{R}}_{abcd}$, is defined by $[\hat{\mathcal{D}}_a, \hat{\mathcal{D}}_b]v^c = \hat{\mathcal{R}}_{abd}{}^c v^d$, similar to the definition of the full covariant Riemann tensor \mathcal{R}_{abcd} but with a conventional opposite sign, and the calculations for the projected Ricci tensor $\hat{\mathcal{R}}_{ab}$ and projected Ricci scalar $\hat{\mathcal{R}}$ just follow the same way as in GR) as

$$\hat{\mathcal{R}} \doteq \frac{\kappa(\rho + 3p) - f}{F} - \frac{2}{3} \left[\theta + \frac{3\dot{F}}{2F} \right]^2 - \frac{2\hat{\mathcal{D}}^2 F}{F}. \quad (4.24)$$

The spatial derivative of this projected Ricci scalar, $\eta_a \equiv \frac{1}{2}a\hat{\mathcal{D}}_a\hat{\mathcal{R}}$, is then obtained after a lengthy calculation as

$$\begin{aligned}\eta_a &= \frac{a}{2F}\kappa(\hat{\mathcal{D}}_a\rho + 3\hat{\mathcal{D}}_ap) - \frac{a}{F}\left[\frac{3}{2F}\dot{F} + \theta\right]\hat{\mathcal{D}}_a\dot{F} \\ &\quad - \frac{a}{2F}\hat{\mathcal{D}}_af - \frac{a}{F}\hat{\mathcal{D}}_a(\hat{\mathcal{D}}^2F) - \frac{2a}{3}\left[\frac{3}{2F}\dot{F} + \theta\right]\hat{\mathcal{D}}_a\theta \\ &\quad + \frac{a}{3F}\left[\frac{3}{2F}\dot{F} + \theta\right]\left[\frac{3}{2F}\dot{F} - \theta\right]\hat{\mathcal{D}}_aF,\end{aligned}\quad (4.25)$$

and its time evolution is governed by the propagation equation

$$\begin{aligned}\dot{\eta}_a + \frac{2\theta}{3}\eta_a &= \frac{a}{2F}\left[\frac{3}{F}\dot{F} - \frac{2}{3}\theta\right]\hat{\mathcal{D}}_a\hat{\mathcal{D}}^2F - \frac{a}{F}\kappa\hat{\mathcal{D}}_a\hat{\mathcal{D}}^c q_c \\ &\quad - \frac{a}{F}\hat{\mathcal{D}}_a(\hat{\mathcal{D}}^2F) - \left[\frac{\dot{F}}{F} + \frac{2\theta}{3}\right]a\hat{\mathcal{D}}_a\hat{\mathcal{D}}^c A_c.\end{aligned}\quad (4.26)$$

As we are considering a spatially flat universe, its spatial curvature will vanish for large scales, meaning that $\hat{\mathcal{R}} = 0$. Thus from Eq. (4.24) we have

$$\left[\frac{1}{3}\theta + \frac{\dot{F}}{2F}\right]^2 = \frac{1}{6F}[\kappa(\rho + 3p) - f].\quad (4.27)$$

This is just the modified (first) Friedmann equation in the $f(R)$ version of gravitational theory, and the other modified background equations (the second Friedmann equation and the energy-conservation equation) could be obtained by taking the zeroth-order parts of Eqs. (4.17) and (4.19). It is easy to check that when $f(R) = R$, we have $F = 1$, and these equations just reduce to those in GR – in this case GR and the Palatini- $f(R)$ theory lead to the same results.

Remember that we have had f , F and R as functions of \mathcal{T} at hand, it is then straightforward to calculate \dot{F} , \ddot{F} , $\hat{\mathcal{D}}_aF$, $\hat{\mathcal{D}}_a\dot{F}$ etc. as functions of $\dot{\mathcal{T}} \doteq -(\rho_b + \rho_c)\theta$ and $\hat{\mathcal{D}}_a\mathcal{T} = (1 - 3c_s^2)\hat{\mathcal{D}}_a\rho_b + \hat{\mathcal{D}}_a\rho_c$, in which $\rho_{b(c)}$ is the energy density of baryons (cold dark matter) and c_s is the baryon sound speed. Note that in this work we choose to neglect the small baryon pressure except in the terms where its spatial derivative is involved, in which case they might be significant at small scales. The above equations could then be numerically propagated given

the initial conditions, to obtain the evolutions of small density perturbations and the CMB and matter power spectra in theories of $f(R)$ gravity. Finally the three-year WMAP data on CMB spectra, SNLS SN data and SDSS data on matter power spectrum could be used to constrain parameters in the $f(R)$ models. These results will be given in the following section.

4.3 Numerical Results and Cosmological Constraints

This section is devoted to numerical results and constraints of the present model. To this effect we will first very briefly summarize and explain the effects of the $f(R)$ modifications to GR on the linear spectra; for more details see [61]. After that we shall employ the public Markov Chain Monte Carlo (MCMC) engine [37] to search the parameter space with the theoretical CMB and matter power spectra calculated by the modified CAMB code; the constraints are then summarized and discussed.

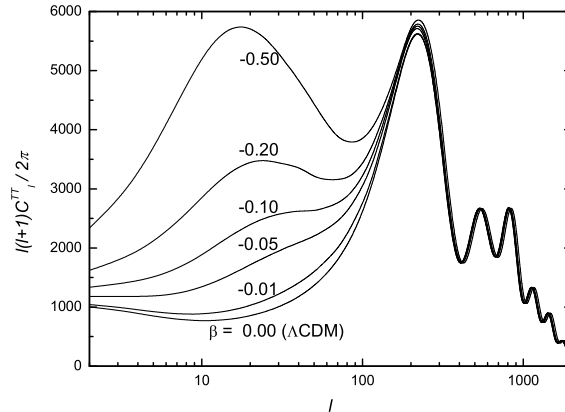


Figure 4.1: The TT CMB spectrum for the $f(R) = R + \alpha(-R)^\beta$ model, with Ω_m (current fractional energy density of nonrelativistic matter) and H_0 (current Hubble constant) fixed to be 0.3 and 72 km/s/Mpc respectively. Choices of β are indicated besides the curves. The case $\beta = 0$ corresponds to a Λ CDM Universe.

In Fig. 4.1 we have displayed the TT CMB spectra for the model with different choices of β . It is obvious from this figure that, when $\beta < 0$, the spectrum gets a boost in the scales $l \leq 100$, which could be significant if $|\beta|$ is large enough. This effect is due to a strong late-time integrated Sachs-Wolfe (ISW) effect [61, 66], which in turn originates from the unusually rapid late-time decay of the gravitational potential ϕ of the present $f(R)$ model compared with Λ CDM, as shown in the lower panel of Fig. 3 in [61] (see this reference for more details). We have not given the curves for $\beta > 0$ because in that case the spectrum generally blows up except for very small $|\beta|$ s (see below).

Another interesting feature in Fig. 4.1 is that for negative β the spectrum shifts towards the right-hand-side (larger l 's), likely due to the unusual angular-distance-redshift relation [67, 27]. Since the standard Λ CDM cosmology is expected to be valid in the early times when the correction to GR is negligible, the sound horizon and the thickness of the last scattering surface are the same as in Λ CDM. But at late times the Friedmann equation is modified (Eq. (4.27)), and so is the relation between redshift and conformal distance. This would cause the CMB spectrum to shift sideways. This shifting effect, however, is negligible for the constrained ranges of β obtained below.

The CMB EE polarization and cross correlation spectra show no additional interesting features and cannot be used to put strong constraint on the model parameters, and so we will not present and discuss them here.

We have also given in Fig. 4.2 the matter power spectra. As indicated in this figure, the matter power spectrum depends sensitively on the value of β and could differ from Λ CDM significantly even if $|\beta|$ only deviates from 0 by a tiny amount *e.g.*, of order $\mathcal{O}(10^{-5})$. This feature has been pointed out and discussed extensively in [58, 57, 61]. Basically, this is because of the sensitive response of the modified gravity to the spatial variations of matter distribution, which, at small enough scales would significantly affect the growth of density perturbations. To be explicit, for large enough k 's, the growth equation for

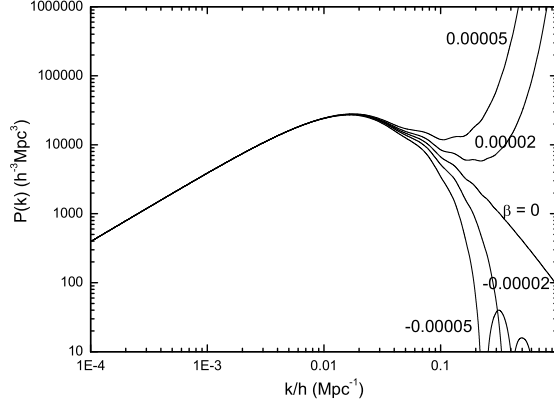


Figure 4.2: The matter power spectra of the $f(R) = R + \alpha(-R)^\beta$ model for different choices of β (both negative and positive) as indicated beside the curves. The case $\beta = 0$ corresponds to a Λ CDM Universe.

the comoving energy density fluctuations δ_m could be written as [57]

$$\frac{d^2 \delta_m}{dN^2} \doteq -\frac{k^2}{a^2 H^2} \frac{\dot{F}}{3F(2FH + \dot{F})} \delta_m, \quad (4.28)$$

in which $N \equiv \log(a)$ and $\dot{F}/3F(2FH + \dot{F}) = c_{s,eff}^2$ acts as an effective sound speed squared that vanishes in the Λ CDM model. For the present $f(R)$ model, we have $F = 1 - \alpha\beta(-R)^{\beta-1}$, in which α and $-R$ are positive and $-R$ decreases with time. So if $\beta < 0$, then $\dot{F} > 0$ and thus $c_{s,eff}^2 > 0$; this effective pressure term will restrict the growths of small-scale density perturbations and leads to oscillations (as shown in Fig. 4.2 for the case of $\beta = -0.00005$) of the spectrum in these scales. On the other hand, if $\beta > 0$ (as we hope to recover standard Λ CDM cosmology in earlier times, we shall also restrict ourselves to $\beta < 1$), then \dot{F} and $c_{s,eff}^2$ will be negative; this will make the density fluctuations unstable and blow up, the same reason why the CMB spectrum depends so sensitively on positive β s.

Since from Figs. 4.1 and 4.2 we have seen that the linear spectra of our $f(R)$ model depend very sensitively on the model parameter β , it can be expected that the data on CMB and matter power spectra could place stringent constraints on β , as we will show now. As mentioned in Sec. 4.1, we shall

firstly use the full three year WMAP data and then perform a joint constraint simultaneously using WMAP, SNLS and SDSS data to constrain the parameters.

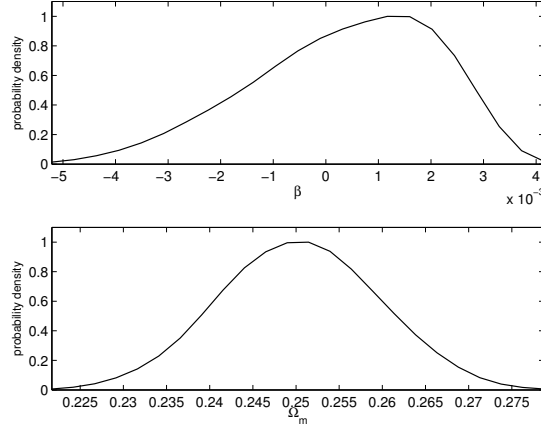


Figure 4.3: The marginal distributions of Ω_m and β , obtained using the three year WMAP data alone. Here the distributions are normalized such that the maximum probability density is 1.

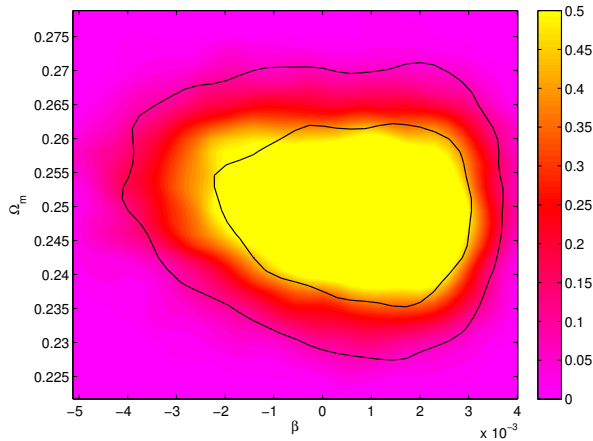


Figure 4.4: The contour plot of the joint distribution of Ω_m and β , constrained by WMAP data alone. The inner and outer loops are the 68% and 95% confidence contours respectively.

Because the Hubble parameter H_0 is already measured to rather good precision by the HST Key Project, we shall use $H_0 = 72$ km/s/Mpc [1] in our calculations. Therefore we vary the following parameters: baryon density

$\omega_b = \Omega_b h^2$, cold dark matter $\omega_c = \Omega_c h^2$, reionization redshift z_{re} , spectral index n_s , normalization amplitude A_s and the model parameter β . In Fig. 4.3 the marginal distributions of Ω_m and β are shown. The 95% confidence interval for Ω_m and β are $[0.233, 0.268]$ and $[-3.45 \times 10^{-3}, 3.07 \times 10^{-3}]$ respectively. We also present the contour plot of the joint distribution of Ω_m and β in Fig. 4.4. From these figures we can see that the CMB spectra could constrain $|\beta|$ to $\mathcal{O}(10^{-3})$, ~ 100 times more stringent than the constraint from the CMB shift parameter [53], which is of order 0.1. That the CMB spectra is much more powerful in constraining the parameters than the CMB shift parameter is expected because the former bears a lot more information than the latter. It looks from these figures that a slightly positive β is preferred by the CMB data.

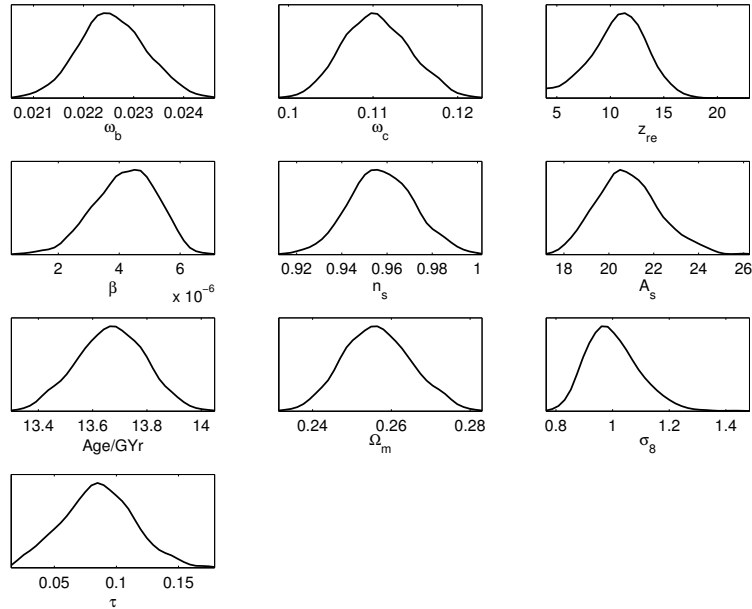


Figure 4.5: The marginal distributions of the various model parameters, constrained simultaneously by the WMAP, SNLS and SDSS data sets. The distributions are normalized such that the maximum probability density is 1.

To tighten the bounds on the parameters, we perform a joint constraint

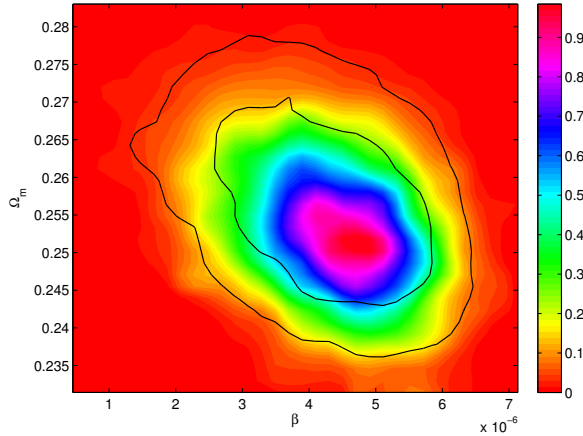


Figure 4.6: The contour plot of joint distribution of Ω_m and β under the constraints of the WMAP, SNLS and SDSS data sets. The inner and outer loops are the 68% and 95% confidence contours respectively.

making use of both the three-year WMAP and the SDSS data sets. In addition to the matter power spectrum, the SNe data from SNLS [68] is also used in the joint constraint, though their effects are found to be negligible. For the SDSS data, we conservatively adopt the measurements for scales larger than $k = 0.2h \text{ Mpc}^{-1}$ (where $h \equiv H_0/(100 \text{ km s}^{-1}\text{Mpc}^{-1})$) to avoid encountering the nonlinear effects in the measured matter power spectrum. The bias between galaxy power spectrum and matter power spectrum is assumed to be a scale independent constant; CosmoMC [37] assumes a flat prior on it and marginalizes analytically.

The calculation indicates that indeed the allowed range is shrunk, as indicated in Figs. 4.5 and 4.6 (for completeness in Fig. 4.7 we have also plotted the best-fitted curves with the observational data points from SNLS, WMAP and SDSS we use in the constraints). The 95% confidence intervals for Ω_m and β now become $[0.241, 0.274]$ and $[2.12 \times 10^{-6}, 5.98 \times 10^{-6}]$ respectively, and the 95% confidence interval for σ_8 is $[0.85, 1.21]$. The distribution of Ω_m does not change much since it is already well constrained by the WMAP, but the bound on β is tightened to the order of 10^{-6} (and obviously future refined

data could still further this constraint). What is more, these joint constraints also prefer a positive β and actually have excluded the case of $\beta = 0$, *i.e.*, the Λ CDM paradigm, at the 95% confidence level. In Fig. 4.7 we could see that all the data sets are fitted very well. Furthermore, more stringent constraints on β can be obtained if data points in the nonlinear regime are also used since the matter power spectrum will blow up in the small scales for positive β (see Fig. 4.2). Nonetheless, our stringent constraint on β already makes the model nearly indistinguishable from Λ CDM for practical purposes, and without a natural motivation for such tiny values of β this model should be more reasonably disfavored.

4.4 Discussion and Conclusion

In conclusion, we have in this work derived the perturbation equations for general theories of Palatini- $f(R)$ gravity and applied them to a typical class of model $f(R) = R + \alpha(-R)^\beta$ which is proposed as an alternative to the cosmological constant to account for the late-time accelerating cosmic expansion and has been extensively studied. We then calculate the CMB and matter power spectra for this model using a modified CAMB code. It is shown that for negative β s the potential ϕ will see an unusually rapid decay at late times, leading to an enhancement of the ISW effect and thus a boost of the TT CMB spectrum at small ls . There also appears a positive effective pressure term in the equation governing the growth of density perturbations, which could be significant for small scales (large ks) and restricts the perturbation growths in these scales. For positive β s, however, the small-scale density fluctuations will become unstable and grow exponentially, resulting in blowing-ups of the matter power spectrum.

We have constrained the model parameters using the WMAP, SNLS and SDSS data. Because the CMB and matter power spectra are rather sensitive to

the exact values of the parameter β , we are able to give much more stringent constraints on β ($\mathcal{O}(10^{-3})$ and $\mathcal{O}(10^{-6})$ respectively) than those ($\mathcal{O}(10^{-1})$) coming from the CMB shift parameter fitting or measurements on SNIa [53]. Compared with the bound ($\mathcal{O}(10^{-5})$) from SDSS data alone [57], our WMAP + SNLS + SDSS constraint is tighter because the allowed range of Ω_m is largely reduced here.

These constraints seem to make the present model (in its allowed parameter space) indistinguishable from the Λ CDM paradigm and raise a fine-tuning problem to the late $f(R)$ gravity theory. However, there still remains the interesting possibility that $f(R)$ modification of gravity enters at earlier times (or higher densities): can it survive the tests from WMAP and SDSS data? This topic is beyond the scope of this article and has been investigated in another work [61]; in that case the parameter space for $f(R)$ gravity is also highly limited.

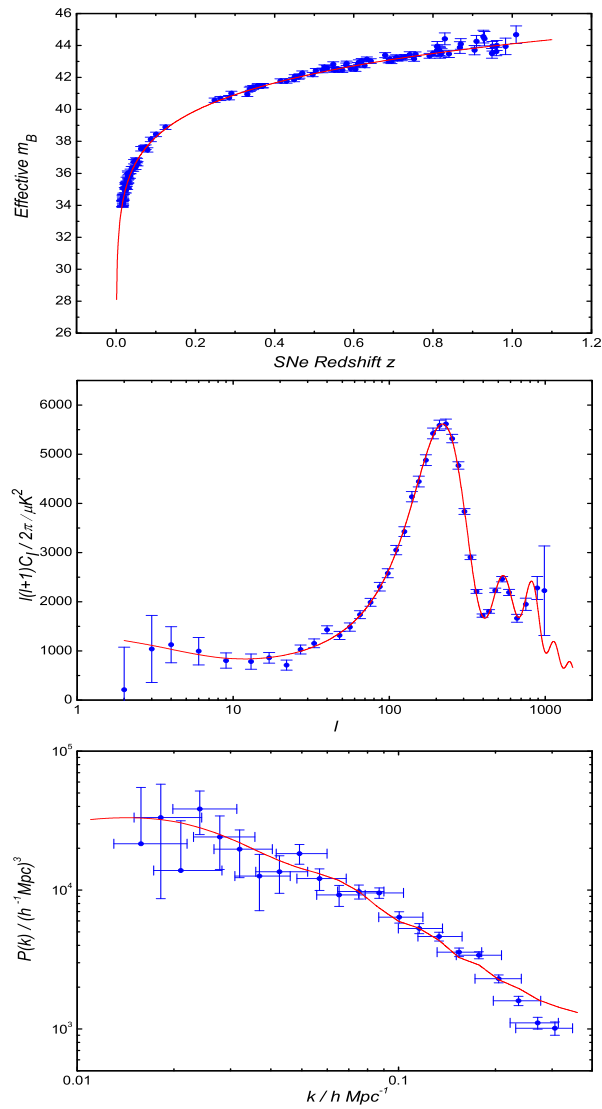


Figure 4.7: The data points from SNLS (upper panel), WMAP (middle panel) and SDSS (lower panel) data sets against the theoretical curves of our best-fitted model. For SDSS data we have plotted both vertical and horizontal error bars. Note that the last three data points from SDSS (for which $k > 0.2h \text{ Mpc}^{-1}$) are not included in our numerical constraints, and we have used a bias of 1.1 to relate the best fit theoretical power spectrum to the SDSS data.

Chapter 5

CMB Constraint on Radion Evolution in the Brane World Scenario

The brane world model is a very popular type of extra dimension model motivated by string theory. In many versions of brane model, the modulus field of extra dimensions, the radion, could have cosmological evolution, which induces variation of the Higgs vacuum expectation value, $\langle H \rangle$, resulting in cosmological variation of the electron mass m_e . The formation of Cosmic Microwave Background (CMB) anisotropies is thus affected, causing changes both in the peaks positions and amplitudes in the CMB power spectra. In this Chapter we shall make use of the WMAP data to constrain the evolution of the radion. This Chapter is duplicated from our article in arXiv ¹ [69].

This Chapter is organized as follows. Section 5.1 is the introduction. In Section 5.2, we carry out the conventional dimensional reduction to get the radion dependence of various constants. We shall see that only the Higgs VEV is expected to vary in the context of brane world models. We then describe the effect of variation of Higgs VEV on the CMB power spectra in Section 5.3.1. The numerical constraints on the radion (or Higgs VEV) are

¹K. C. Chan and M.-C Chu, arXiv: 07060391

presented in Section 5.3.2. We summarize in Section 5.4.

5.1 Introduction

Investigations in string/M theory suggest the existence of extra dimensions. In particular, we may live in a brane world in a bulk of dimensions greater than 4. In this brane world picture, the matter fields are confined on the brane which is a (1+3)-dimensional hypersurface embedded in the bulk, while gravity can propagate freely in the whole extended universe. For a review on extra dimensions and brane worlds see *e.g.* [70, 71]. By restricting the standard model particles on the brane, brane world models have evaded the strong constraints on the size of extra dimensions. Up till now Newtonian gravity is only tested to submillimeter scale [72], and existence of extra dimensions below this scale remains possible. From the phenomenological point of view, extra dimensions open a new door to address the hierarchy problem, the large scale discrepancy between the Planck scale and the electroweak scale [73]. For example, in the Randall-Sundrum two-brane model [74], one can obtain a large scale discrepancy by fine-tuning the interbrane distance, the radion; thus some mechanisms have to be invoked to stabilize the radion [75].

There are many moduli fields in string theory and the radion is an example. The moduli fields have to be stabilized so as not to upset the limits from long range force experiments and tests of general relativity. Other than invoking stabilization potentials, there could also be some attractor mechanism that drives the theory towards general relativity [76]. The radion may also act as a chameleon field and acquire mass by self-interactions to avoid the most restrictive of current bounds [77, 78]. If these scenarios hold, it is possible that the radion still evolves after the epoch of Big Bang Nucleosynthesis (BBN).

Studies of brane world models can be divided into two main streams. On

one hand, more complex models are studied in order to strengthen the connection between string theories and brane models; on the other hand, efforts are made to confront brane models with observational data [79]. In the brane world scenario, evolving radion induces variation of Higgs VEV, and therefore constraining the evolution of the radion implies limiting the evolution of Higgs VEV. In Ref. [80, 81], the constraints on the evolution of the radion are obtained from BBN and the best fit to the observational abundances of D, ${}^4\text{He}$ and ${}^7\text{Li}$ suggests a small variation in the radion during BBN compared to its present value. Molecular spectral lines can be used to determine $\mu \equiv m_p/m_e$ [27]. Recently, Reinhold *et al.* used quasar H_2 spectral lines to obtain $\Delta\mu/\mu = (2.4 \pm 0.6) \times 10^{-5}$ for a weighted fit [82]. The constraints on μ can be interpreted as an indication that the Higgs VEV (and hence the radion) at redshift 2–3, was different from its value today. The Cosmic Microwave Background (CMB) anisotropies are measured with high precision by WMAP [4, 38] and other observations. Thus it is timely to study the effects of the existence of extra dimensions on CMB and fill the “redshift gap” between BBN and quasar constraints using data from CMB. In this article we shall use the three-year WMAP data to constrain the evolution of the radion.

Within the brane world scenario, an extra term, called the dark radiation term, appears in the modified Friedmann equations [83], and it causes great difficulty in calculating the Sachs-Wolfe Effect [84, 85]. Nonetheless, in this work we will constrain the radion evolution through the variation of constants caused by the variation of Higgs VEV ignoring the dark radiation term. CMB has been used to constrain the Higgs VEV using the pre-WMAP data in [86]. However it is desirable to get an improved bound using the high precision three-year WMAP data, including the polarization power spectrum. We also demonstrate that the constraints can be tightened substantially if we make use of HST measurement of H_0 .

5.2 Dimensional Reduction and Low Energy Effective Actions

In this section we will start from the higher dimensional action and carry out the dimensional reduction to derive the dependence of the constants on the radion. There are many works on effective actions in extra dimensions, *e.g.* [76, 87, 88], and the formalism here follows closely that in Ref. [89, 80]. We shall dimensionally reduce the higher dimensional gravitational action to obtain its low energy effective action first. The higher dimensional action reads

$$S = \int d^{4+n} X \sqrt{-G} \left[\left(\frac{1}{2\kappa_{4+n}^2} {}^{(4+n)}R \right) + \mathcal{L}_m \right], \quad (5.1)$$

where n denotes the number of compact extra dimensions, and X^A represents the bulk spacetime coordinate, $A = 0, 1, \dots, 3 + n$. The higher dimensional Ricci scalar is denoted by ${}^{(4+n)}R$, and G is the determinant of the full spacetime metric G_{AB} . \mathcal{L}_m is the matter field Lagrangian density, which may include scalar fields, vector boson fields and Dirac fermion fields.

To proceed we shall take the metric ansatz

$$ds^2 = G_{AB} dX^A dX^B = g_{\mu\nu}(x) dx^\mu dx^\nu + h_{ij}(x) dy^i dy^j. \quad (5.2)$$

In this metric the Greek indices run over 0, 1, 2 and 3, while the Latin indices i and j run over the extra dimensions from 4 to $3 + n$. We are only interested in the zero-mode of the Kaluza Klein expansion, and so the extra dimensional metric $h_{ij}(x)$ does not depend on the extra dimension coordinate. Furthermore, we have assumed that the metric in Eq. 5.2 is block-diagonal because the vector-like connection G_μ^i vanishes for zero-mode [89]. The extra dimensions are compactified on an orbifold and the dimensionless coordinate y^i assumes values in the interval $[0,1]$. Using the ansatz Eq. 5.2, it is easy to get

$$\sqrt{-G} = \sqrt{-g} \sqrt{h}, \quad (5.3)$$

where g and h are the determinants of $g_{\mu\nu}$ and h_{ij} respectively. After some calculations, $^{(4+n)}R$ can be expressed in terms of the 4D Ricci scalar $^{(4)}R$ as

$$\begin{aligned} ^{(4+n)}R &= ^{(4)}R - g^{\rho\sigma} \partial_\rho (h^{ij} \partial_\sigma h_{ij}) + \frac{1}{4} g^{\rho\sigma} \partial_\rho h^{ij} \partial_\sigma h_{ij} \\ &\quad - \frac{1}{4} g^{\rho\sigma} h^{ij} \partial_\rho h_{ij} h^{kl} \partial_\sigma h_{kl}. \end{aligned} \quad (5.4)$$

We also define

$$\frac{1}{\kappa_4^2} \equiv \frac{\mathcal{V}_0}{\kappa_{4+n}^2}, \quad (5.5)$$

where \mathcal{V}_0 is the volume of the extra dimensions today. Thus S can be written as

$$\begin{aligned} S &= \int d^4x d^n y \sqrt{-g} \sqrt{h} \left[\frac{1}{2\kappa_4^2 \mathcal{V}_0} \left(^{(4)}R + \frac{1}{4} g^{\rho\sigma} \partial_\rho h^{ij} \partial_\sigma h_{ij} \right. \right. \\ &\quad \left. \left. + \frac{1}{4} g^{\rho\sigma} h^{ij} \partial_\rho h_{ij} h^{kl} \partial_\sigma h_{kl} \right) + \mathcal{L}_m \right], \end{aligned} \quad (5.6)$$

after integration by parts once. We shall work in the Einstein frame with pure Ricci scalar in the gravitational action. To do so we will apply the conformal transformation

$$\tilde{g}_{\mu\nu} = e^{-2\theta} g_{\mu\nu} \quad (5.7)$$

with

$$e^{-2\theta} = \frac{\sqrt{h}}{\mathcal{V}_0}. \quad (5.8)$$

After some algebra, we obtain the effective action

$$\begin{aligned} S &= \int d^4x \sqrt{-\tilde{g}} \left[\frac{1}{2\kappa_4^2} \left(^{(4)}R + \frac{1}{4} \tilde{g}^{\rho\sigma} \partial_\rho h^{ij} \partial_\sigma h_{ij} \right. \right. \\ &\quad \left. \left. - \frac{1}{8} \tilde{g}^{\rho\sigma} h^{ij} \partial_\rho h_{ij} h^{kl} \partial_\sigma h_{kl} \right) + e^{4\theta} \mathcal{L}_m \right]. \end{aligned} \quad (5.9)$$

For concreteness, we further assume that the extra dimensional manifold is homogeneous and isotropic. Hence the extra dimension metric takes the simple form:

$$\text{diag}(b^2, b^2, \dots, b^2). \quad (5.10)$$

With the ansatz Eq. 5.10, the action Eq. 5.9 reduces to

$$S = \int d^4x \sqrt{-\tilde{g}} \left[\frac{1}{2\kappa_4^2} {}^{(4)}R - \frac{n(n+2)}{4\kappa_4^2} \frac{1}{b^2} \tilde{g}^{\mu\nu} \partial_\mu b \partial_\nu b + e^{4\theta} \mathcal{L}_m \right]. \quad (5.11)$$

To make the scalar field canonical, we define a new scalar field, the radion σ , as

$$\sigma \equiv \frac{1}{\kappa_4} \sqrt{\frac{n+2}{2n}} \ln \frac{b^n}{\mathcal{V}_0}. \quad (5.12)$$

Finally the effective action reads

$$S = \int d^4x \sqrt{-\tilde{g}} \left[\frac{1}{2\kappa_4^2} \left({}^{(4)}R - \frac{1}{2} \tilde{g}^{\mu\nu} \partial_\mu \sigma \partial_\nu \sigma \right) + e^{4\theta} \mathcal{L}_m \right]. \quad (5.13)$$

We now study the matter sector in more details. Although the matter fields only live on the brane, their actions are still affected by the existence of extra dimensions because of the conformal transformation Eq. 5.7. Let us begin with the minimally coupled scalar field

$$S_{\text{Scalar}} = \int d^4x \sqrt{-g} \left(-\frac{1}{2} g^{\mu\nu} \partial_\mu \phi \partial_\nu \phi - V(\phi) \right). \quad (5.14)$$

After the conformal transformation Eq. 5.7, it becomes

$$\begin{aligned} S_{\text{Scalar}} &= \int d^4x \sqrt{-\tilde{g}} \left[-\frac{1}{2} \exp \left(-\kappa_4 \sigma \sqrt{\frac{2n}{n+2}} \right) \tilde{g}^{\mu\nu} \partial_\mu \phi \partial_\nu \phi \right. \\ &\quad \left. - \exp \left(-2\kappa_4 \sigma \sqrt{\frac{2n}{n+2}} \right) V(\phi) \right]. \end{aligned} \quad (5.15)$$

To turn the kinetic term into the canonical form, we make a change of variable:

$$\Phi = \exp \left(-\kappa_4 \sigma \sqrt{\frac{n}{2(n+2)}} \right) \phi. \quad (5.16)$$

We then recover the standard scalar field action

$$S_{\text{Scalar}} = \int d^4x \sqrt{-\tilde{g}} \left[-\frac{1}{2} \tilde{g}^{\mu\nu} \partial_\mu \Phi \partial_\nu \Phi - \exp \left(-2\kappa_4 \sigma \sqrt{\frac{2n}{n+2}} \right) V(\phi) \right]. \quad (5.17)$$

If $V(\phi)$ is taken to be a simple renormalizable potential of the form

$$V(\phi) = \frac{1}{2} \mu^2 \phi^2 + \frac{1}{4} \nu \phi^4, \quad (5.18)$$

we then have

$$V(\Phi) = \frac{1}{2} \exp \left(-\kappa_4 \sigma \sqrt{\frac{2n}{n+2}} \right) \mu^2 \Phi^2 + \frac{1}{4} \nu \Phi^4. \quad (5.19)$$

We see that the mass of the scalar field is dependent on the radion in the Einstein frame for both signs of μ^2 . One of the most important scalar fields in particle physics is the Higgs field. Masses of the fermions and quarks can be generated by their Yukawa couplings to the Higgs field. In this mechanism, the fermion masses are proportional to the Higgs VEV, $\langle H \rangle$. Thus we get the radion dependence of the fermion mass

$$m \propto \langle H \rangle \propto \exp \left(-\frac{\kappa_4}{2} \sigma \sqrt{\frac{2n}{n+2}} \right). \quad (5.20)$$

For the gauge field, the action is given by

$$S_{\text{Gauge}} = -\frac{1}{4g_*^2} \int d^4x \sqrt{-g} g^{\mu\rho} g^{\nu\sigma} F_{\mu\nu} F_{\rho\sigma}, \quad (5.21)$$

where $F_{\mu\nu}$ is the gauge-invariant field strength tensor. However the action is invariant under the conformal transformation Eq. 5.7, and so the effective 4D coupling constant is the same as the higher dimensional g_*^2 .

Similar techniques can be applied to the Dirac field ψ with mass \hat{m} [90]:

$$S_{\text{Dirac}} = \int d^4x \sqrt{-g} (i\bar{\psi} e^{i\mu} \gamma_i D_\mu \psi - \hat{m} \bar{\psi} \psi), \quad (5.22)$$

where $e^{i\mu}$ is the vierbein and D_μ is the covariant derivative. After the transformation Eq. 5.7, we have

$$\begin{aligned} S_{\text{Dirac}} &= \int d^4x \sqrt{-\tilde{g}} \left[\exp \left(-\frac{3}{2} \kappa_4 \sigma \sqrt{\frac{2n}{n+2}} \right) i\bar{\psi} \tilde{e}^{i\mu} \gamma^i \tilde{D}_\mu \psi \right. \\ &\quad \left. - \hat{m} \exp \left(-2\kappa_4 \sigma \sqrt{\frac{2n}{n+2}} \right) \bar{\psi} \psi \right]. \end{aligned} \quad (5.23)$$

We get the canonical action

$$\begin{aligned} S_{\text{Dirac}} &= \int d^4x \sqrt{-\tilde{g}} \left[i\bar{\Psi} \tilde{e}^{i\mu} \gamma^\mu \tilde{D}_\mu \Psi \right. \\ &\quad \left. - \hat{m} \exp \left(-\frac{\kappa_4}{2} \sigma \sqrt{\frac{2n}{n+2}} \right) \bar{\Psi} \Psi \right] \end{aligned} \quad (5.24)$$

by redefining the field ψ as

$$\Psi = \exp\left(-\frac{3\kappa_4}{4}\sigma\sqrt{\frac{2n}{n+2}}\right)\psi. \quad (5.25)$$

We can read out the radion dependence of the fermion mass, which is the same as Eq. 5.20.

Thus, for the brane world models in the Einstein frame, only the fermion masses, among other fundamental constants, acquire radion dependence and are expected to vary. Or, in the framework of Standard Model, we may say that only $\langle H \rangle$ is radion-dependent while the Yukawa coupling is constant.

5.3 Numerical Constraints on the Evolution of the Radion

In the last section, we see that only $\langle H \rangle$ is expected to vary in the brane world scenario. Here we first discuss the effects of variation of $\langle H \rangle$ on the CMB power spectra, and then we present the numerical constraints on $\langle H \rangle$ and the radion using the the three-year WMAP data.

5.3.1 Effects of Variation of Higgs VEV on CMB Power Spectra

The variation of $\langle H \rangle$ induces changes in the Fermi constant G_F , the quark masses, the nucleon binding energy and the electron mass m_e [91]. The variation of G_F is not relevant in the epoch of CMB recombination. We can also ignore the changes in strong nuclear force and nuclear binding energy caused by the variation of quark mass. Since the baryon mass is dominated by the QCD scale parameter Λ_{QCD} , and the quark masses contribute at only a few percents level, we shall neglect the influence of $\langle H \rangle$ on the baryon mass. Thus

the variation in $\langle H \rangle$ boils down to variation of m_e [92], which modifies the recombination history.

The variation of m_e enters CMB through the binding energies of hydrogen, H_I , and helium, He_{II} , Thomson cross-section σ_T , and the recombination coefficients α and the two-photon decay rates of hydrogen and helium. In the Appendix C, we list the evolution equations and modifications to take care of variations of m_e . Here we only sketch the modifications to be made. The binding energies scale as m_e , σ_T is proportional to m_e^{-2} , and the two-photon decay rates vary as m_e [93]. For α , one can derive a differential equation relating the matter temperature T_M and m_e [92], through which the dependence of α on m_e can be deduced using the empirical fitting of α as a function of T_M in the literature.

Among these effects caused by the variation of m_e , the change in the binding energy of hydrogen is most significant on the power spectra; less important is the effect of Thomson cross-section, while the effects of the recombination coefficients and two-photon rates are small.

For convenience, we define

$$\rho \equiv \frac{\langle H \rangle_{\text{CMB}}}{\langle H \rangle_0}, \quad (5.26)$$

where $\langle H \rangle_{\text{CMB}}$ and $\langle H \rangle_0$ denote the Higgs VEV in the era of CMB recombination and today respectively.

Shown in Fig. 5.1 is the CMB temperature power spectrum with ρ being 1, 1.05 and 0.95 respectively with the other parameters being the standard ones.

We see that both the positions and amplitudes of the peaks change for $\rho = 1.05$ and 0.95 in comparison with $\rho = 1$. For $\rho = 1.05$ (0.95), because the binding energy $\propto m_e$ and it dictates the epoch of CMB recombination, CMB recombination takes place at an earlier (later) time. Therefore the sound horizon is smaller (larger), and the distance to the last scattering surface is larger (smaller); the peaks shift to the larger (smaller) l scales. The change in

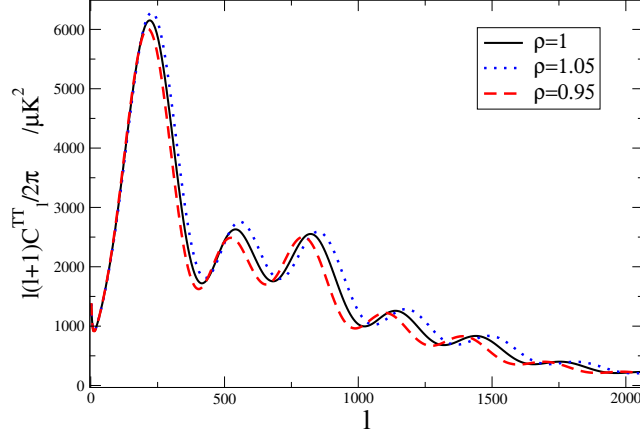


Figure 5.1: The CMB temperature power spectrum with $\rho=1$, 1.05 and 0.95 respectively. Other cosmological parameters assume the standard values.

amplitudes is due to early Integrated Sachs–Wolfe (ISW) effect and damping effect. For $\rho = 1.05$ (0.95), the residual radiation is higher (lower) right after recombination, which gives an enhanced (reduced) early ISW effect and hence the first peak is boosted (diminished). Early recombination also means greater Hubble rate and narrower visibility function at decoupling time, and thus the damping is reduced and the power in high l scales is enhanced.

Shown in Fig. 5.2 is the E -polarization power spectrum with $\rho=1$, 1.05 and 0.95 respectively. The main features of this power spectrum can be understood with the tight coupling semi-analytic formula for the polarization strength Θ_{Pl} of a particular k mode [8]:

$$\Theta_{Pl}(k) \simeq \frac{5k\Theta_1(k, \eta_*)}{6\dot{\tau}(\eta_*)} \frac{l^2}{[k(\eta_0 - \eta_*)]^2} j_l(k(\eta_0 - \eta_*)), \quad (5.27)$$

where η_0 and η_* are the conformal times of today and the last-scattering surface respectively. $\Theta_1(k, \eta_*)$ is the dipole of the photon distribution. Again, for larger m_e , recombination occurs at an earlier conformal time, and because the spherical Bessel function peaks at $l \sim k(\eta_0 - \eta_*)$, the peaks shift to the larger l s. The power of the peaks is higher because the dipole, which is like the velocity of a fluid in the tight coupling limit, is larger at the earlier time.

In the above discussions, we have assumed that m_e is constant in the whole

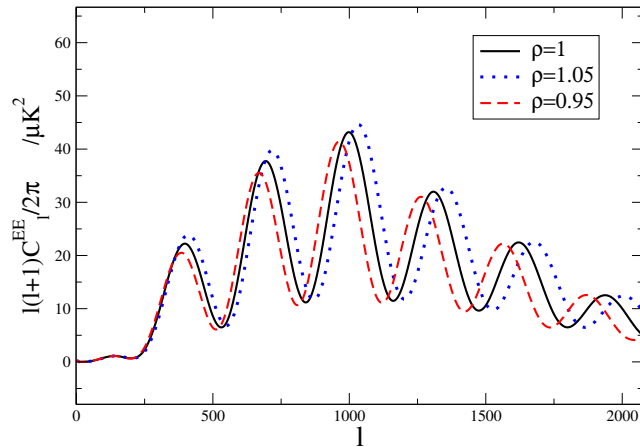


Figure 5.2: The CMB E -polarization power spectrum with $\rho=1$, 1.05 and 0.95 respectively. Other cosmological parameters assume the standard values.

calculation. Because the effect of m_e on CMB is only important near the decoupling time, even if we assume that m_e evolves, *e.g.* as a linear function of the scale factor a , only the value of m_e at the decoupling time matters. Thus CMB indeed gives the constraint on m_e at $z \sim 1000$.

5.3.2 Numerical Constraints on the Higgs VEV and Radion by CMB

In this section, we constrain the range of $\langle H \rangle$ (or radion) using the three-year WMAP data [4, 38]. To do so, we make use of the Markov Chain Monte Carlo (MCMC) method (see Appendix A for introduction) implemented by the engine CosmoMC [37], which searches for the maximum of the likelihood function. The theoretical CMB spectra are calculated by the Boltzmann code CMBFAST [36]. We vary the following set of parameters: the Hubble parameter, H_0 , the baryon density, $\omega_b = \Omega_b h^2$ ($h = H_0/100 \text{ km s}^{-1} \text{ Mpc}^{-1}$), the cold dark matter density, $\omega_c = \Omega_c h^2$, the reionization redshift, z_{re} , the primordial fluctuation amplitude, A_s , the spectral index, n_s , and ρ . Flatness of the universe is assumed in all the calculations.

The marginal distributions of the parameters are shown in Fig. 5.3.

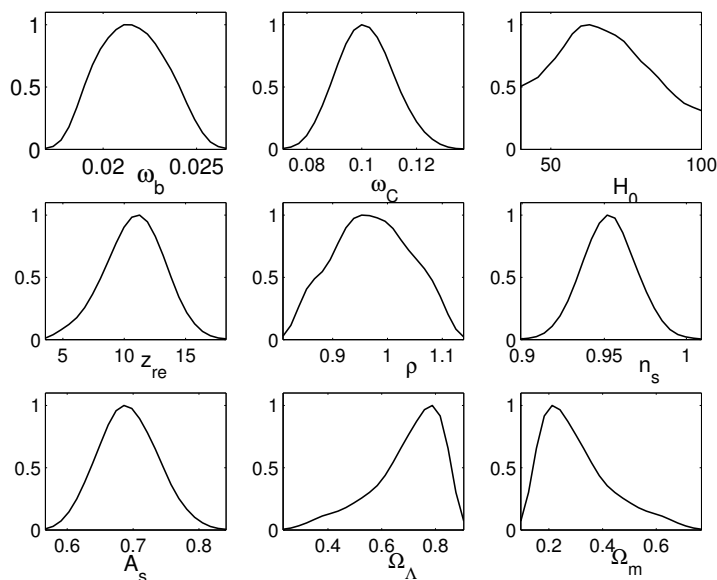


Figure 5.3: The marginal distributions of the free parameters, constrained by the three-year WMAP data. In addition to the free parameters $\omega_b \equiv \Omega_b h^2$, $\omega_c = \Omega_c h^2$, H_0 , z_{re} , n_s , A_s and ρ , shown also are the derived distributions of the density parameter of matter (Ω_m) and cosmological constant (Ω_Λ). The Hubble parameter is allowed to vary in the range from 40 to 100 $\text{km s}^{-1} \text{Mpc}^{-1}$ (we will suppress this unit afterwards). Here and thereafter, the maxima of the distributions are arbitrarily normalized to 1.

In particular, the 95% confidence interval (C. I.) for ρ is [0.85, 1.11]. The constraint is relatively weak. Most of the other standard cosmological parameters are well constrained in the usual ranges, except the Hubble parameter. Although the mean of H_0 being 67.6 is still close to the “canonical” value 72, its distribution spreads wide. This suggests that H_0 may be degenerate with ρ . To see the degeneracy between ρ and other parameters explicitly, we display the contour marginal distributions of various cosmological parameters plotted versus ρ in Fig. 5.4.

Among the parameters, ω_b and ω_c show slight degeneracy with ρ , but ρ is strongly degenerate with H_0 . This suggests that we may obtain a tighter bound if we use the measurement of H_0 by the HST Key Project to break the degeneracy between H_0 and ρ . We carry out the MCMC run once again but

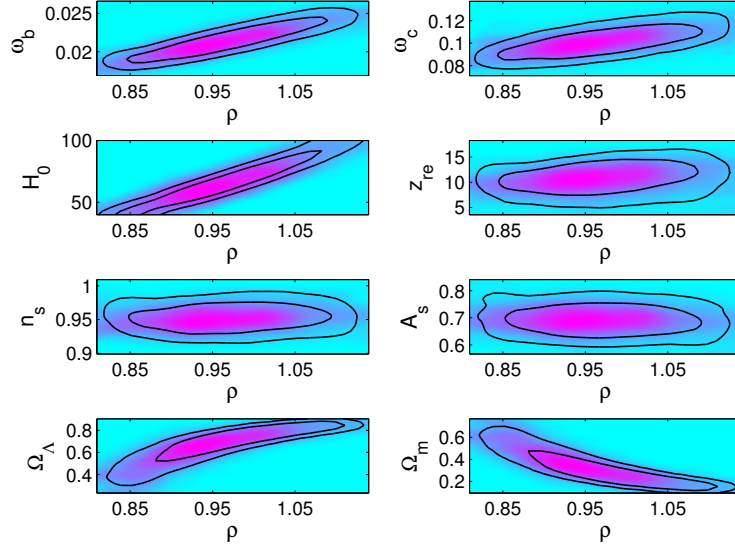


Figure 5.4: The contour marginal distributions of cosmological parameters plotted against ρ . Among the free parameters, H_0 is the most strongly degenerate with ρ .

with $H_0 = 72$ [1]. Indeed, the bounds on ρ are tightened substantially, as can be seen in Fig. 5.5. The 95% C. I. now becomes $[0.97, 1.02]$.

Using Eq. 5.20, we get the change of the radion

$$\sigma_{\text{CMB}} - \sigma_0 = -\frac{2}{\kappa_4} \sqrt{\frac{2n}{n+2}} \ln \rho, \quad (5.28)$$

which is proportional to $\ln \rho$. In Fig. 5.6, we show the derived distribution of $\ln \rho$.

One sees again that the spread of the distribution of $(\sigma_{\text{CMB}} - \sigma_0)$ for H_0 being allowed to vary from 40 to 100 is much larger than that for fixed $H_0 = 72$, and their 95% C. I. are $[-0.094, 0.17]$ and $[-0.019, 0.034]$ respectively.

The constraint on Higgs VEV by CMB is first deduced in [86] using pre-WMAP data sets. There is no marked difference between their constraint $0.92 < \rho < 1.13$ and ours with H_0 being allowed to vary in the interval $40 < H_0 < 100$. The small difference may be due to the use of different data sets and/or statistical methods. The data set we used is the recent three-year WMAP data with the polarization spectrum [4, 38] while the pre-WMAP

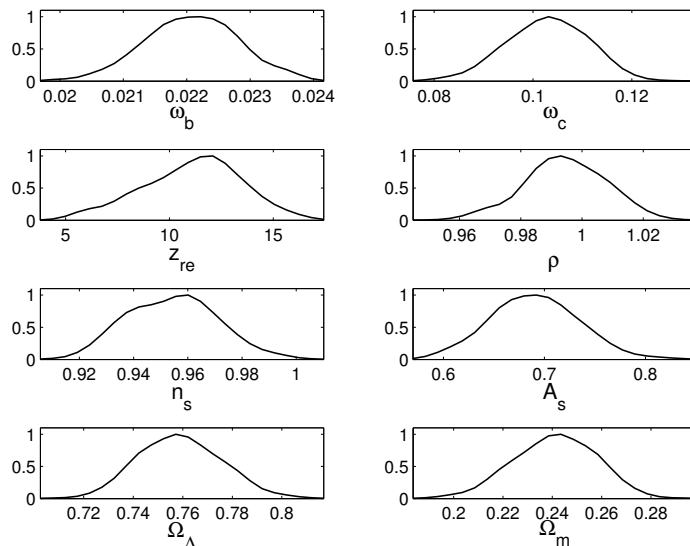


Figure 5.5: Same as Fig. 5.3, but with H_0 fixed to be 72. The spread of ρ is much smaller than that in Fig. 5.3.

temperature power spectrum is used in [86]. They restricted H_0 in the interval [50, 80] and more importantly Ω_M in the interval [0.3, 0.4], which is a small portion of the distribution in Fig. 5.6. We also allow for two more free parameters, z_{re} and A_s in our MCMC runs. That's why we get bounds comparable to theirs although we use more accurate data set. Moreover, we show that the bounds on ρ can be tightened substantially if the HST measurement of H_0 is used.

Since the upcoming Planck satellite mission is going to measure the temperature power spectrum to as high as $l \sim 2500$ and the E -polarization spectrum to $l \sim 1500$, we expect that there will be tremendous improvement in the constraint on ρ . We can forecast the improvement that Planck will bring quantitatively using the Fisher matrix, which has been widely used to predict the expected uncertainties in future experiments (see Appendix B). Under the assumption of Gaussian perturbations and Gaussian noise, the Fisher matrix

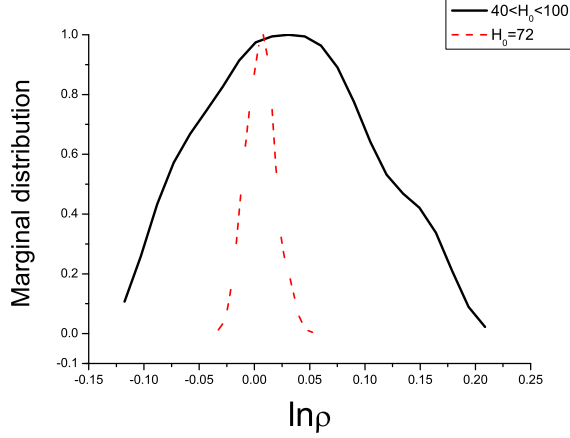


Figure 5.6: The derived marginal distributions of $\ln \rho = -\frac{\kappa_A}{2} \sqrt{\frac{n+2}{2n}} (\sigma_{\text{CMB}} - \sigma_0)$ for $40 < H_0 < 100$ (solid line) and $H_0 = 72$ (dashed line) respectively. Note that the latter has much smaller spread.

takes the form

$$F_{ij} = \sum_l \sum_{X,Y} \frac{\partial C_{Xl}}{\partial p_i} (\text{Cov}_{lXY})^{-1} \frac{\partial C_{Yl}}{\partial p_j}, \quad (5.29)$$

where p_i is the i th free parameter and C_{Xl} is the l th multipole of the observed spectrum of type X , which can be the temperature, temperature-polarization and E-polarization spectra. The experimental precision is encoded in the covariant matrix Cov_{lXY} . With the expected Planck power spectra, the constraint on ρ is tightened by a factor of 7 when H_0 is allowed to vary; the current constraint with H_0 fixed will be tightened by a factor of 5.

We compare the present CMB constraints with other constraints in Table 5.1. We note that the BBN constraint and the quasar absorption line constraint are of opposite signs. Even if both constraints are found to be correct, that does not immediately rule out the evolution of the radion since the radion may stabilize to its present value in an oscillatory manner. If this is the case, we may find that the radion takes a value very close to 1 near the epoch of CMB recombination. Unfortunately, the current CMB data is not discriminating enough. With the forthcoming Planck data, the CMB constraint will

be tightened substantially and may tell us if this interesting scenario holds or not.

Redshift z	Observations	95 % C. I. for $(\langle H \rangle_z - \langle H \rangle_0)/\langle H \rangle_0$, where $\langle H \rangle_z$ denotes the value of Higgs VEV at redshift z
10^{10}	BBN [80]	[0.00,0.04]
1000	CMB	H_0 free: [-0.15,0.11]; $H_0=72$: [-0.03, 0.02]
2-3	Quasar absorption lines [82]	Weighted fit: $-0.9 \times [1.8 \times 10^{-5}, 3.0 \times 10^{-5}]^2$

Table 5.1: The present constraints on the variation of $\langle H \rangle$ at various redshifts. The CMB constraint fills the gap in the “redshift ladder” in between BBN and quasar. The future Planck data will tighten the CMB constraint (so that it is compatible with other constraints.)

5.4 Conclusion

In the brane world scenario, the evolution of radion induces variation of $\langle H \rangle$. Among its consequences, we expect only the variation of m_e to be relevant in the epoch of CMB recombination. Variation of m_e changes the time of CMB recombination, causing changes in both the peak positions and amplitudes of the CMB power spectra. Thus we can constrain the radion evolution via limiting the variation of $\langle H \rangle$ using the CMB data. With the three-year WMAP data and H_0 as a free parameter, we obtain the 95% C. I. for ρ to be [0.85, 1.11]; when we fix H_0 to be the HST result $72 \text{ km s}^{-1} \text{ Mpc}^{-1}$ the constraint for ρ is tightened to be [0.97, 1.02]. In terms of $\ln \rho$, which is proportional to the change in radion σ by Eq. 5.28, the corresponding 95% C. I.’s are [-0.094, 0.17] and [-0.019, 0.034] respectively. Although the current CMB data is not discriminating enough, the upcoming Planck data should tighten the bounds by a factor of 5 or so.

Chapter 6

Summary of the Thesis

We have witnessed the transition of cosmology from a data-starved subject to the era of precision cosmology. Large volume and high precision data are obtained from SNe Ia surveys, measurements of the primordial nucleus abundances, CMB anisotropy probes and galaxy surveys. Among these pillars of modern cosmology, the CMB observations are particularly fruitful. The CMB temperature power spectrum has been extended from first tens multipoles measured by COBE in 1992 to $l \sim 1000$ measured by WMAP now. The polarization power spectrum has been detected and will be more accurate in the future.

CMB is formed 3.8×10^5 years after the birth of the universe, and so it provides us with very important information about the early universe. It enables us to constrain physics in the early universe. The small initial perturbations justify the use of linear analysis, which makes CMB calculations simple and clean.

In this thesis, we have used the WMAP data, sometimes together with other data as well, to constrain physics beyond the “standard model”. We have constrained the variation of the gravitational constant G , a particular parametrization of $f(R)$ gravity in the Palatini formalism and the radion evolution in the brane world scenario by limiting the variation of m_e . Here is the summary of our key results.

In Chapter 3, we use the CMB power spectra to constrain the cosmological variation of gravitational constant G . It is found that the sensitivity of CMB anisotropies to the variation of G is enhanced when G is required to converge to its present value. The variations of G from the CMB decoupling epoch $z \sim 1000$ to the present time are modeled by a step function and a linear function of scale factor a respectively, and the corresponding 95% confidence intervals for G/G_0 are $[0.95, 1.05]$ and $[0.89, 1.13]$, G_0 being the present value. The CMB constraint is unique in the sense that it entails the range of redshift from $z \approx 1000$ to 0.

In Chapter 4, we make use of the covariant and gauge invariant perturbation equations in general theories of $f(R)$ gravity in the Palatini formalism to linear order and calculate the CMB and matter power spectra for an extensively discussed model, $f(R) = R + \alpha|R|^\beta$, which is a possible candidate for the late-time cosmic accelerating expansion found recently. These spectra are discussed and found to be sensitively dependent on the value of β . We are thus able to make stringent constraints on β from cosmological data on CMB and matter power spectra. The three-year WMAP data alone gives a constraint $|\beta| \lesssim \mathcal{O}(10^{-3})$ while the joint WMAP, Supernova Legacy Survey (SNLS) and Sloan Digital Sky Survey (SDSS) data sets tightens this to $\beta \sim \mathcal{O}(10^{-6})$, about an order of magnitude more stringent than the constraint from SDSS data alone, which makes this model practically indistinguishable from the standard Λ CDM paradigm.

Finally, in Chapter 5, we use the WMAP data to constrain the evolution of the extra dimension volume, the radion, in brane model. In many versions of brane model, the radion could have cosmological evolution, which induces variation of the Higgs vacuum expectation value, $\langle H \rangle$, resulting in cosmological variation of the electron mass m_e . The formation of CMB anisotropies is thus affected, causing changes both in the peaks positions and amplitudes in the CMB power spectra. Using the three-year WMAP CMB data, with the

Hubble parameter H_0 fixed to be the HST result $72 \text{ km s}^{-1} \text{ Mpc}^{-1}$, we obtain a constraint on ρ , the ratio of the value of $\langle H \rangle$ at CMB recombination to its present value, to be $[0.97, 1.02]$.

The above summarizes the major work in my MPhil studies, but it is just the tip of an iceberg of the exciting interplay between modern cosmology and the fundamental physics. As we proceed from precision cosmology to accuracy cosmology, more excitements are expected to come.

Appendix A

Markov Chain Monte Carlo

Method

We shall introduce the Markov Chain Monte Carlo (MCMC) method in this appendix. We first give the general ideas of MCMC, and then the Metropolis-Hastings algorithm is introduced. Lastly, we discuss the multiple chain convergence diagnostics for test of convergence. For more detailed introduction and overview, see [94, 95].

A.1 Basic Theory of MCMC

A Markov chain is defined as a series of random variables $X^{(0)}, X^{(1)}, X^{(2)}, \dots$, in which the influence of $X^{(0)}, \dots, X^{(n)}$ on $X^{(n+1)}$ is explicitly through $X^{(n)}$ only. Mathematically, it is

$$P(x^{(n+1)}|x^{(n)}, \{x^{(t)} : t \in \mathcal{E}\}) = P(x^{(n+1)}|x^{(n)}), \quad (\text{A.1})$$

where \mathcal{E} is any subset of $\{0, \dots, n-1\}$.

A Markov chain can be specified by giving the initial probability distribution of various states $X^{(0)}$ and a rule for each state to evolve into other states. The rule is a conditional distribution, $T_n(X^{(n)}, X^{(n+1)})$, which assigns $X^{(n+1)}$ given the n th step distribution of the states, $X^{(n)}$. In other

words, $T_n(X^{(n)}, X^{(n+1)})$ gives the transition probabilities from every state to all other states. If the transition probabilities are independent of step n , it is called homogeneous (or stationary) and it is simply denoted by T . Thus for a homogeneous chain with initial distribution $X^{(0)}$, the n th step distribution is $X^{(n)} = T^n X^{(0)}$.

For a distribution $\pi(x)$, if the transition probabilities $T_n(x, x')$ satisfy

$$\pi(x) = \sum_{x'} T_n(x', x)\pi(x'), \quad (\text{A.2})$$

for all n , then π is said to be invariant with respect to the Markov chain with transition probabilities $T_n(x', x)$. A Markov chain has at least one invariant distribution. We want to construct the transition probabilities such that the distribution which we aim to sample from is invariant. This is desirable because ever since the invariant distribution is reached, the Markov chain will sample from the distribution forever. In practice, the Markov chains are often constructed to be time-reversible homogeneous, *i.e.*,

$$T(x, x')\pi(x) = T(x', x)\pi(x'). \quad (\text{A.3})$$

This is equivalent to saying that the Markov chain satisfies detailed balance. Eq. A.3 is a sufficient condition for being invariant as

$$\begin{aligned} \sum_{x'} T(x', x)\pi(x') &= \sum_{x'} T(x, x')\pi(x) \\ &= \pi(x) \sum_{x'} T(x, x') \\ &= \pi(x). \end{aligned} \quad (\text{A.4})$$

However, an invariant chain does not necessarily satisfy detailed balance.

Because for each train, we have to pick an initial distribution by hand, the results are meaningful if the target distribution $\pi(x)$ is reached irrespective of the initial conditions. Thus, in addition to being invariant, we also require the Markov chain to be ergodic:

$$\lim_{n \rightarrow \infty} X^{(n)} = \pi, \quad (\text{A.5})$$

for all choices of $X^{(0)}$. In this definition, the asymptotic distribution is unique and is called the equilibrium distribution.

Loosely speaking, if a homogeneous Markov chain on a finite state space with positive transition probabilities for all states has an invariant distribution, it is ergodic. However to show convergence is not always easy, and we shall discuss convergence diagnostics using multiple chains in Section A.3.

A.2 The Metropolis-Hastings Algorithm

The Metropolis-Hastings algorithm is one of the simplest and most popular realization of MCMC. It samples from the target distribution by repeatedly generating random points in the parameter space. In CosmoMC [37], MCMC is implemented by the Metropolis-Hastings algorithm.

The Metropolis-Hastings transition kernel is constructed as follows. Suppose the chain is at $x^{(n)}$ of the parameter space. A candidate point x^* is proposed by changing certain component(s) of $x^{(n)}$. The change is drawn from a proposed distribution $q(x^{(n)}, x^*)$, which in general may not be symmetric. The proposed new point is accepted with probability

$$\alpha(x^{(n)}, x^*) = \min \left(1, \frac{P(x^*)q(x^*, x^{(n)})}{P(x^{(n)})q(x^{(n)}, x^*)} \right), \quad (\text{A.6})$$

where $P(x)$ is the posterior distribution that we want to sample from. Therefore a successful transition to a point x^* has to be proposed and accepted, and the transition probability $T(x^{(n)}, x^*)$ is

$$T(x^{(n)}, x^*) = q(x^{(n)}, x^*)\alpha(x^{(n)}, x^*). \quad (\text{A.7})$$

If x^* is accepted, it is assigned to $x^{(n+1)}$; otherwise $x^{(n+1)}$ assumes the value of $x^{(n)}$.

If the proposal density is symmetric, the acceptance probability $\alpha(x^{(n)}, x^*)$ depends on the ratio of the posterior probabilities only. Then it basically

means that if $P(x^*) > P(x^{(n)})$, the proposed step is taken; otherwise a random number u is drawn from a uniform distribution in $[0,1)$, and the step is accepted if $u < \frac{P(x^*)}{P(x^{(n)})}$, or else it is rejected.

One can verify that this construction satisfies the detailed balance Eq. A.3:

$$\begin{aligned} P(x^*)T(x^*, x^{(n)}) &= P(x^*)q(x^*, x^{(n)}) \min \left[1, \frac{P(x^{(n)})q(x^{(n)}, x^*)}{P(x^*)q(x^*, x^{(n)})} \right] \\ &= \min [P(x^*)q(x^*, x^{(n)}), P(x^{(n)})q(x^{(n)}, x^*)] \end{aligned} \quad (\text{A.8})$$

Noting that the last line is symmetric between $x^{(n)}$ and x^* , we can conclude that it is equal to $P(x^{(n)})T(x^{(n)}, x^*)$.

A.3 Convergence Diagnostics

The target invariant distribution is sampled from only if convergence is attained. Thus convergence must be checked before useful statistical measures can be computed from the Markov chains. Among the convergence tests, multiple chain test advocated by Gelman *et al.* (see [96, 97]) are very popular today, mainly because of its simplicity and ease to implement in codes.

In this methods, we suppose M chains are launched with widely separated initial starting points in the parameter space. For each chain, there are $2N$ steps. The first N steps are ignored to avoid the “burn-in” period. We can compute the means and variances from the rest of the chains to see if the chains are indistinguishable.

Let y_i^j denote the i th iteration of the last N steps of the chain j . The mean of the chain j is

$$\bar{y}^j = \frac{1}{N} \sum_{i=1}^N y_i^j, \quad (\text{A.9})$$

and the mean of all the chains is

$$\bar{y} = \frac{1}{NM} \sum_{j=1}^M \sum_{i=1}^N y_i^j. \quad (\text{A.10})$$

We also define the variance among the chains as

$$\frac{B}{N} = \frac{1}{M-1} \sum_{j=1}^M (\bar{y}^j - \bar{y})^2, \quad (\text{A.11})$$

and the average of variances within a chain as

$$W = \frac{1}{M(N-1)} \sum_{j=1}^M \sum_{i=1}^N (y_i^j - \bar{y}^j)^2. \quad (\text{A.12})$$

From these variances, a quantity

$$\hat{R} = \frac{\left(\frac{N-1}{N}W + \frac{B}{N}\right) + \frac{B}{MN}}{W} \quad (\text{A.13})$$

can be constructed as a measure of convergence of the chains (see [96] for motivation of the expression). The numerator is an estimate of the variance if the distribution is stationary; otherwise it is an overestimate. The denominator is an underestimate of the variance if convergence is not yet reached. Thus \hat{R} is usually greater than 1, and convergence can be assumed if it is close to 1, such as 1.05.

Appendix B

Forecast by Fisher Matrix

The Fisher matrix has been widely used to forecast the precision of future cosmological experiments. For example, the Fisher matrix method has been used in [40, 98, 33] to forecast future constraints. In this thesis, it is useful for us to predict the improvement in the constraints that the forthcoming Planck satellite mission will bring. One can refer to Ref. [99] for a comprehensive review on Fisher matrix, but for lucid introduction, we again recommend Dodelson's book [8].

Suppose that there is a true underlying power spectrum C_l depending on a set of parameters λ_i , and C_l^{obs} denotes the experimentally observed one, the error of which is represented by σ_l :

$$\sigma_l = \sqrt{\frac{2}{(2l+1)f_{\text{sky}}}} (C_l + w^{-1}B_l^2). \quad (\text{B.1})$$

The first term, proportional to C_l , is the cosmic variance; the second term is due to noise, atmospheric or instrumental. More precisely, w^{-1} represents the detector noise level and B_l is the beam width function. The prefactor $2l+1$ comes from the fact that there are $2l+1$ m -modes, and hence $2l+1$ independent samples. However, experiment only observes a fraction of the sky, f_{sky} , which therefore accounts for reduction in the sample size.

We can compute the χ^2

$$\chi^2(\lambda_i) = \sum_l \frac{(C_l(\lambda_i) - C_l^{\text{obs}})^2}{\sigma_l^2}. \quad (\text{B.2})$$

We suppose that χ^2 is minimized (or the likelihood is maximized) for $\lambda = \lambda_0$. The derivatives are evaluated at the fiducial model $\lambda = \lambda_0$. We further assume that, around the minimum, χ^2 can be approximated as quadratic. This is equivalent to approximating the errors of C_l by the Gaussian distribution. The Gaussian assumption yields the curvature matrix

$$\begin{aligned} \mathcal{F}_{ij} &= \frac{1}{2} \frac{\partial^2 \chi^2}{\partial \lambda_i \partial \lambda_j} \\ &= \sum_l \frac{1}{\sigma_l^2} \left[\frac{\partial C_l}{\partial \lambda_i} \frac{\partial C_l}{\partial \lambda_j} + (C_l - C_l^{\text{obs}}) \frac{\partial^2 C_l}{\partial \lambda_i \partial \lambda_j} \right]. \end{aligned} \quad (\text{B.3})$$

We shall drop the second term in the square bracket since $C_l - C_l^{\text{obs}}$ is sometimes positive and sometimes negative; its overall contribution is small relative to the first term. Hence we write the curvature matrix as the Fisher matrix

$$F_{ij} = \sum_l \frac{1}{\sigma_l^2} \frac{\partial C_l}{\partial \lambda_i} \frac{\partial C_l}{\partial \lambda_j}. \quad (\text{B.4})$$

This matrix includes the precision of an experiment (σ_l) and the sensitivity of the power spectrum to the parameters (the derivative of C_l). For the constraint on the parameters to be tight, we need high experimental precision (small σ_l) and C_l to change rapidly when the λ_i deviates from λ_{0i} slightly.

So far we have considered only one type of power spectrum. Generalization to more than one yields

$$F_{ij} = \sum_l \sum_{X,Y} \frac{\partial C_{Xl}}{\partial \lambda_i} (\text{Cov}_l)_{XY}^{-1} \frac{\partial C_{Yl}}{\partial \lambda_j}, \quad (\text{B.5})$$

where X and Y may denote temperature, E -polarization, TE cross and B -polarization power spectra and, $(\text{Cov}_l)^{-1}$ is the covariant matrix.

The standard deviation (1 σ error bar) in measuring a parameter λ_i is related to the Fisher information matrix by

$$\sigma_i = \sqrt{(F^{-1})_{ii}}. \quad (\text{B.6})$$

If some of the parameters are known, then only the sub-matrix formed by the unknown parameters needs to be inverted. For example, suppose all the

parameters except λ_i are known, the standard error of λ_i is simply given by $1/\sqrt{F_{ii}}$. By the Cramér-Rao inequality, the estimate of error bar by the Fisher matrix is the lower bound attained by any best unbiased estimator.

Appendix C

Modified Equations in RECFAST with Variation m_e

In this Appendix we list the evolution equations for calculating the ionization history with the effect of modified m_e taken into account. The detailed evolution of the ionization fraction x_e can be modeled by the simple Peebles recombination [7], which is basically a two-level approximation, or using RECFAST [100], the evolution equations of which have been checked against more detailed multi-level calculations. We use a modified RECFAST which allows for variation of m_e to evaluate the evolution of x_e , as in Ref. [101]. The ionization history can be modeled by evolving the ionization fraction of H, x_p , ionization fraction of HeI, x_{HeI} and the matter temperature T_M (see [100] for details):

$$\frac{dx_p}{dz} = \frac{C_H}{H(z)(1+z)} \left[x_e x_p n_H \alpha_H - \beta_H (1 - x_p) \exp\left(-\frac{h\nu_{\text{H}2s}}{kT_M}\right) \right] \quad (\text{C.1})$$

with

$$C_H = \frac{1 + K_H \Lambda_H n_H (1 - x_p)}{1 + K_H (\Lambda_H + \beta_H) n_H (1 - x_p)}, \quad (\text{C.2})$$

$$\frac{dx_{\text{HeII}}}{dz} = \frac{C_{\text{HeII}}}{H(z)(1+z)} \left[x_{\text{HeII}} x_e n_H \alpha_{\text{HeI}} - \beta_{\text{HeI}} (f_{\text{He}} - x_{\text{HeII}}) \exp\left(-\frac{h\nu_{\text{HeI}2s}}{kT_M}\right) \right], \quad (\text{C.3})$$

with

$$C_{\text{HeII}} = \frac{1 + K_{\text{HeI}} \Lambda_{\text{He}} n_{\text{H}} (f_{\text{He}} - x_{\text{HeII}}) \exp\left(-\frac{h\nu_{\text{HeI}2\text{p}-2\text{s}}}{kT_M}\right)}{1 + K_{\text{HeI}} (\Lambda_{\text{He}} + \beta_{\text{HeI}}) n_{\text{H}} (f_{\text{He}} - x_{\text{HeII}}) \exp\left(-\frac{h\nu_{\text{HeI}2\text{p}-2\text{s}}}{kT_M}\right)}, \quad (\text{C.4})$$

and

$$\frac{dT_M}{dz} = \frac{8\sigma_T a_R T_R^4}{3m_e c H(z)(1+z)} \frac{x_e}{1 + f_{\text{He}} + x_e} (T_M - T_R) + \frac{2T_M}{1+z}. \quad (\text{C.5})$$

The meanings of the symbols are in order. In these equations, z is the redshift and $H(z)$ is the Hubble expansion rate at z , and n_{H} is the total hydrogen number density. T_R denotes the radiation temperature $T_0(1+z)$.

$\nu_{\text{H}2\text{s}} = c/121.5682$ nm is the Lyman α frequency. For helium, $\nu_{\text{HeI}2\text{s}} = c/60.1404$ nm, and $\nu_{\text{HeI}2\text{p}-2\text{s}}$ denotes $c/58.4334$ nm $- c/60.1404$ nm, the frequency difference between $\text{HeI } 2^1\text{p}$ and $\text{HeI } 2^1\text{s}$. $K_{\text{H}} \equiv (121.5682 \text{ nm})^3/[8\pi H(z)]$ and $K_{\text{HeI}} \equiv (58.4334 \text{ nm})^3/[8\pi H(z)]$ give the amount of cosmological redshiftings of 2^1p to 1^1s photons. These frequency ν dependent quantities need to be modified as $\nu \propto m_e$.

Λ_{H} and Λ_{He} denote the two-photon decay rates from 2^1s to 1^1s for H and He respectively, and they scale as m_e [93].

The Thomson cross-section σ_T scales as m_e^{-2} as $\sigma_T = 8\pi e^4/(3m_e^2 c^4)$.

α_{H} (α_{HeI}) is the recombination coefficient of H_I (He_{II}), and the photoionization β_{H} (β_{HeII}) is related to it by

$$\beta = \alpha \left(\frac{2\pi m_e kT_M}{h^2} \right)^{3/2} \exp\left(\frac{-h\nu_{2\text{s}}}{kT_M}\right). \quad (\text{C.6})$$

The recombination coefficient α can be expressed as [102]

$$\alpha = \sum_{n,l}^* 8\pi(2l+1) \left(\frac{kT_M}{2\pi m_e} \right)^{\frac{3}{2}} \exp\left(\frac{B_n}{kT_M}\right) \int_{\frac{B_n}{kT_M}}^{\infty} \frac{\sigma_{nl} y^2 dy}{e^y - 1}, \quad (\text{C.7})$$

where B_n is the binding energy of the n th state and σ_{nl} is the ionization cross-section. The asterisk indicates that the sum should be regulated. Using the

fact that B_n scales with m_e and the ionization cross-section scales as m_e^{-2} [27], we can derive [92]

$$\frac{\partial \alpha}{\partial m_e} = -\frac{1}{m_e} \left(2\alpha + T_M \frac{\partial \alpha}{\partial T_M} \right). \quad (\text{C.8})$$

In the literature α is usually parametrized as a function of T_M in the fitting formula. The m_e dependence of α can be extracted from the fitting formula using Eq. C.8 and hence also the m_e dependence of β .

Bibliography

- [1] W. L. Freedman *et al.*, *Astrophys. J.* **553**, 47 (2001).
- [2] R. A. Knop *et al.*, *Astrophys. J.* **598**, 102 (2003).
- [3] S. Burles, K. M. Nollett, and M. S. Turner, Big-Bang Nucleosynthesis: Linking Inner Space and Outer Space, astro-ph/9903300.
- [4] G. Hinshaw *et al.*, Three-Year Wilkinson Microwave Anisotropy Probe (WMAP) Observations: Temperature Analysis, astro-ph/0603451v2.
- [5] M. Tegmark *et al.*, Cosmological Constraints from the SDSS Luminous Red Galaxies, astro-ph/0608632v2.
- [6] J. A. Peacock, *Cosmological Physics*, Cambridge University Press, Cambridge, 1999.
- [7] P. J. E. Peebles, *Principles of Physical Cosmology*, Princeton University Press, New Jersey, 1993.
- [8] S. Dodelson, *Modern Cosmology*, Academic Press, New York, 2003.
- [9] M. Trodden and S. M. Carroll, TASI Lectures: Introduction to Cosmology, astro-ph/0401547 v1.
- [10] A. J. S. Hamilton, Power Spectrum Estimation I. Basics, astro-ph/0503603.

- [11] A. G. Riess *et al.*, *Astron. J.* **116**, 1009 (1998).
- [12] S. Perlmutter *et al.*, *Astrophys. J.* **517**, 565 (1999).
- [13] D. J. Fixsen *et al.*, *Astrophys. J.* **473**, 576 (1996).
- [14] S. M. Carroll, *Living Rev. Rel.* **4**, 1 (2001).
- [15] T. Padmanabhan, *Phys. Rept.* **380**, 235 (2003).
- [16] P. J. E. Peebles and B. Ratra, *Rev. Mod. Phys.* **75**, 559 (2003).
- [17] W. Hu and S. Dodelson, *Annu. Rev. Astron. Astrophys.* **40**, 171 (2002),
astro-ph/0110414.
- [18] W. Hu, *Annals Phys.* **303**, 203 (2003), astro-ph/0210696.
- [19] Y.-T. Lin and B. D. Wandelt, *Astropart. Phys.* **25**, 151 (2006), astro-
ph/0409734v2.
- [20] K. C. Chan and M.-C. Chu, *Phys. Rev. D* **75**, 083521 (2007).
- [21] P. A. M. Dirac, *Nature* **139**, 323 (1937).
- [22] J. G. Williams, X. X. Newhall, and J. O. Dickey, *Phys. Rev. D* **53**, 6730
(1996).
- [23] D. B. Guenther, L. M. Krauss, and P. Demarque, *Astrophys. J.* **498**,
871 (1998).
- [24] S. Degl’Innocenti, G. Fiorentini, G. G. Raffelt, B. Ricci, and A. Weiss,
Astron. Astrophys. **312**, 345 (1996).
- [25] S. E. Thorsett, *Phys. Rev. Lett.* **77**, 1432 (1996).
- [26] F. S. Accetta, L. M. Krauss, and P. Romanelli, *Phys. Lett. B* **248**, 146
(1990).

- [27] J.-P. Uzan, *Rev. Mod. Phys.* **75**, 403 (2003).
- [28] T. Chiba, Constancy of the Constants of Nature, gr-qc/0110118v2.
- [29] P. Lorén-Aguilar, E. García-Berro, J. Isern, and Y. A. Kubyshin, *Class. Quant. Grav.* **20**, 3885 (2003).
- [30] G. R. Dvali, G. Gabadadze, and M. Porrati, *Phys. Lett. B* **485**, 208 (2000).
- [31] X. Chen and M. Kamionkowski, *Phys. Rev. D* **60**, 104036 (1999).
- [32] R. Nagata, T. Chiba, and N. Sugiyama, *Phys. Rev. D* **69**, 083512 (2004).
- [33] O. Zahn and M. Zaldarriaga, *Phys. Rev. D* **67**, 063002 (2003).
- [34] K. I. Umezu, K. Ichiki, and M. Yahiro, *Phys. Rev. D* **72**, 044010 (2005).
- [35] A. Melchiorri and L. M. Griffiths, *New Astron. Rev.* **45**, 321 (2001), astro-ph/0011147.
- [36] U. Seljak and M. Zaldarriaga, *Astrophys. J.* **469**, 437 (1996).
- [37] A. Lewis and S. Bridle, *Phys. Rev. D* **66**, 103511 (2002).
- [38] L. Page *et al.*, Three-Year Wilkinson Microwave Anisotropy Probe (WMAP) Observations: Polarization Analysis, astro-ph/0603450v2.
- [39] D. N. Spergel *et al.*, Wilkinson Microwave Anisotropy Probe (WMAP) Three Year Results: Implications for Cosmology, astro-ph/0603449v2.
- [40] D. J. Einstein, W. Hu, and M. Tegmark, *Astrophys. J.* **518**, 2 (1999).
- [41] T. Clifton, D. F. Mota, and J. D. Barrow, *MNRAS* **358**, 601 (2005).
- [42] B. Li, K. C. Chan, and M.-C. Chu, CMB and Matter Power Spectra Constraints on $f(R)$ Cosmology in the Palatini Formalism, astro-ph/0610794.

- [43] A. G. Riess *et al.*, *Astron. J* **116**, 1009 (1998).
- [44] A. G. Riess *et al.*, *Astron. J.* **607**, 665 (2004).
- [45] S. M. Carroll *et al.*, *Phys. Rev. D* **71**, 063513 (2005).
- [46] S. Capozziello, V. F. Cardone, and A. Troisi, *Phys. Rev. D* **71**, 043503 (2005).
- [47] S. Nojiri and S. D. Odintsov, Introduction to Modified Gravity and Gravitational Alternative for Dark Energy, hep-th/0601213.
- [48] N. D. Birrell and P. C. W. Davis, *Quantum Fields in Curved Spacetime*, Cambridge University Press, Cambridge, 1982.
- [49] A. D. Dolgov and M. Kawasaki, *Phys. Lett. B* **573**, 1 (2003).
- [50] S. Nojiri and S. D. Odintsov, *Phys. Rev. D* **68**, 123512 (2003).
- [51] D. N. Vollick, *Phys. Rev. D* **68**, 063510 (2003).
- [52] S. Capozziello, V. F. Cardone, and M. Francaviglia, *Gen. Rel. Grav.* **38**, 711 (2006).
- [53] M. Amarzguioui, O. Elgaroy, D. F. Mota, and T. Multamaki, *Astron. Astroph.* **454**, 707 (2006).
- [54] S. Fay, R. Tavakol, and S. Tsujikawa, *Phys. Rev. D* **75**, 063509 (2007).
- [55] A. Borowiec, W. Godlowski, and M. Szydlowski, *Phys. Rev. D* **74**, 043502 (2007).
- [56] T. P. Sotiriou, *Class. Quant. Grav.* **23**, 1253 (2006).
- [57] T. Koivisto, *Phys. Rev. D* **73**, 083517 (2006).
- [58] T. Koivisto and M. Kurki-Suonio, *Class. Quant. Grav.* **23**, 2355 (2004).

- [59] M. Tegmark *et al.*, *Astrophys. J.* **606**, 702 (2004).
- [60] T. P. Sotiriou and S. Liberati, *Annals Phys.* **322**, 935 (2007).
- [61] B. Li and M.-C. Chu, *Phys. Rev. D* **74**, 104010 (2006).
- [62] G. Allemandi, A. Borowiec, and M. Francaviglia, *Phys. Rev. D* **70**, 043524 (2004).
- [63] G. F. R. Ellis and H. V. Elst, *Cargèse Lectures 1998: Cosmological Models*, gr-qc/9812046v4.
- [64] A. Challinor and A. Lasenby, *Astrophys. J.* **513**, 1 (1999).
- [65] A. Lewis, 2000 PhD thesis, <http://www.mrao.cam.ac.uk/~aml1005/cmb> .
- [66] T. Koivisto, H. Kurki-Suonio, and F. Ravndal, *Phys. Rev. D* **71**, 064023 (2005).
- [67] A. Riazuelo and J.-P. Uzan, *Phys. Rev. D* **66**, 023525 (2002).
- [68] P. Astier *et al.*, *Astron. Astroph.* **447**, 31 (2006).
- [69] K. C. Chan and M.-C. Chu, *CMB Constraint on Radion Evolution in the Brane World Scenario*, arXiv: 0706.0391.
- [70] C. Csáki, *TASI Lectures on Extra Dimensions and Branes*, hep-ph/0404096.
- [71] P. Brax and C. van de Bruck, *Cosmology and Brane Worlds: A Review*, hep-th/0303095.
- [72] D. J. Kapner *et al.*, *Phys. Rev. Lett.* **98**, 021101 (2007).
- [73] N. Arkani-Hamed, S. Dimopoulos, and G. Dvali, *Phys. Lett. B* **429**, 263 (1998).

- [74] L. Randall and R. Sundrum, Phys. Rev. Lett. **83**, 3370 (1999).
- [75] W. D. Goldberger and M. B. Wise, Phys. Rev. Lett. **83**, 4922 (1999).
- [76] P. Brax, C. van de Bruck, A.-C. Davis, and C. S. Rhodes, Phys. Rev. D. **67**, 023512 (2003).
- [77] J. Khoury and A. Weltman, Phys. Rev. Lett. **93**, 171104 (2004).
- [78] D. F. Mota and D. J. Shaw, Phys. Rev. D **75**, 063501 (2007).
- [79] M. Deruelle, Astrophys. Space Sci. **283**, 619 (2003), gr-qc/0301035.
- [80] B. Li and M.-C. Chu, Phys. Rev. D **73**, 023509 (2006).
- [81] B. Li and M.-C. Chu, Phys. Rev. D **73**, 025004 (2006).
- [82] E. Reinhold *et al.*, Phys. Rev. Lett. **96**, 151101 (2006).
- [83] P. Binetruy, C. Deffayet, U. Ellwanger, and D. Langlois, Phys. Lett. B **477**, 285 (2000).
- [84] J. D. Barrow and R. Maartens, Phys. Lett. B **532**, 153 (2002).
- [85] K. Koyama, Phys. Rev. Lett. **91**, 221301 (2003).
- [86] J. J. Yoo and R. J. Scherrer, Phys. Rev. D **67**, 043517 (2003).
- [87] S. M. Carroll, J. Geddes, M. B. Hoffman, and R. M. Wald, Phys. Rev. D **66**, 024036 (2002).
- [88] R. Sundrum, Phys. Rev. D **59**, 085009 (1999).
- [89] A. Mazumdar, R. N. Mohapatra, and A. Pérez-Lorenzana, JCAP **0406**, 004 (2004).
- [90] Y. Fujii and K.-I. Maeda, *The Scalar-Tensor Theory of Gravitation*, Cambridge University Press, Cambridge, 2003.

- [91] V. V. Dixit and M. Sher, Phys. Rev. D **37**, 1097 (1988).
- [92] J. Kujat and R. J. Scherrer, Phys. Rev. D **62**, 023510 (2000).
- [93] G. Breit and E. Teller, Astrophys. J. **91**, 215 (1940).
- [94] R. M. Neal, Probabilistic Inference Using Markov Chain Monte Carlo Methods, <http://www.cs.toronto.edu/~radford/ftp/review.pdf>.
- [95] D. J. C. MacKay, *Information Theory, Inference, and Learning Algorithms*, Cambridge University Press, Cambridge, 2003, <http://www.inference.phy.cam.ac.uk/mackay/itila/book.html>.
- [96] S. Brooks and A. Gelman, Journal of Computational and Graphical Statistics **7**, 434 (1998), <http://www.statslab.cam.ac.uk/~steve/mypapers/brog96.ps>.
- [97] L. Verde *et al.*, Astrophys. J. Suppl. **148**, 195 (2003).
- [98] G. Jungman, M. Kamionkowski, and A. Kosowsky, Phys. Rev. Lett. **76**, 1007 (1996).
- [99] M. Tegmark, A. N. Taylor, and A. F. Heavens, Astrophys. J. **480**, 22 (1997).
- [100] S. Seager, D. D. Sasselov, and D. Scott, Astrophys. J. **523**, L1 (1999).
- [101] K. Ichikawa, T. Kanzaki, and M. Kawasaki, Phys. Rev. D **74**, 023515 (2006).
- [102] M. Kaplinghat, R. J. Scherrer, and M. S. Turner, Phys. Rev. D **60**, 023516 (1999).